

de Haas-van Alphen effect study of dislocations in copper*

Y. K. Chang[†] and R. J. Higgins*Department of Physics, University of Oregon, Eugene, Oregon 97403*

(Received 12 May 1975)

The influence of lattice dislocations on conduction electrons has been studied both theoretically and experimentally in copper single crystals. A first-principles de Haas-van Alphen (dHvA) dephasing calculation was made, using the dislocation strain field with a realistic dislocation array. Both the Dingle temperature X , which characterizes the amplitude reduction, and the dHvA relative phase shift were measured using dHvA wave-shape analysis. Breaking the cubic symmetry by introducing a forest of edge dislocations allows a test of the sensitivity of previously equivalent neck orbits to the relative orientation with respect to the dislocation lines. Both magnitude and anisotropy agree with the theory. Orbits in contact with the Brillouin zone were found to have larger X . A slight field dependence predicted by the dephasing calculation was observed. The large discrepancy observed among different $1/\tau$ results obtained from dHvA, radio-frequency size effect, and resistivity measurements is due to the different sensitivity of each method to small-angle scattering by the long-range strain field around dislocations. It is shown how to separate dislocation effects from mosaic-structure effects also present in these strained crystals.

I. INTRODUCTION

The de Haas-van Alphen (dHvA) effect has been used to investigate electron scattering in a dislocated lattice to shed some new light on the old baffling problem of electron scattering by lattice dislocations.^{1,2} Many theories¹⁻⁵ have attempted to bring the theoretical estimates of the dislocation electrical resistivity ρ_d close to the experimental values, which are usually one order of magnitude larger. However, none of these theories are satisfactory, especially in dealing with the core of a dislocation which is believed to have the dominant contribution to ρ_d . Experimentally, the observed values of ρ_d were inconsistent³ and recent findings revealed even more controversies. Contrary to earlier results those observations showed that the dislocation resistivity ρ_d is anisotropic,⁶ and depends on the stage of deformation⁷ and on the method by which the dislocations are introduced⁸ (i.e., on the dislocation configuration in a deformed crystal). Lattice dislocations are sizable line defects which often extend over hundreds of thousands of interatomic spacings, and the strain field of a dislocation decreases slowly from its core in a plane perpendicular to the dislocation line. A microscopic tool such as the dHvA effect can bring detailed information on the scattering, which is averaged out in bulk transport measurements. First, the measurement is local in k space, offering the opportunity to compare different regions of the Fermi surface (FS) with differing sensitivities to strain. Second, the scattering is dominated by the small-angle effects of the long-range strain field, and uncertainties about the core are relatively unimportant.

Basinski, Howie, and Templeton have attempted to study the scattering anisotropy in a bent copper

single crystal by observing four $\langle 111 \rangle$ belly dHvA amplitudes. (Their preliminary results were briefly mentioned in the discussion to Ref. 9.) Their results indicated that the scattering is anisotropic. Unfortunately, no further systematic study was reported since then, mainly owing to the complexity of the problem. Recently Terwilliger and Higgins¹⁰⁻¹² (TH) and Coleridge and Watts¹³ (CW) have measured the Dingle temperature X as a function of dislocation density N_d for several symmetry orbits in copper, and found that dislocations, which have little effect on resistivity, have a large effect on the dHvA Dingle temperature. The TH results, measured on an array of edge dislocations, exhibited a linear dependence of X on N_d and a large orbital anisotropy. Viewed as scattering, their results give a lifetime τ of the order of 10^{-3} times shorter than that obtained from dislocation resistivity. This suggests that most dislocation scattering is by small angles, since τ measures the true lifetime of the Landau level, unweighted by scattering angle as in resistivity. The CW results, measured on randomly oriented dislocations, are similar but their X 's are smaller than those of TH.

TH¹⁰ have proposed a classical scattering model, demonstrating small-angle scattering, which leads to a linear relation between X and N_d and the right direction of the orbital anisotropy. Watts¹⁴ has shown that the dephasing effect due to the dislocation strain field is large enough to account for the measured X , by choosing proper orbit strain sensitivity parameters. However, Watts considered only dilational strain and rotation around a dislocation and did not include the pure shear strain. The calculation was done on two extreme regions, depending on the ratio of orbit size r_c to dislocation spacing d . For $r_c/d \ll 1$, the strain is essentially

constant around an orbit, but each orbit experiences a different strain, *assumed* to be given by a Gaussian distribution. When the dHvA phase is averaged over the sample it yields a field dependence $X \propto N_d/H$. This field-dependent X is a consequence of the *assumed* Gaussian strain distribution (e.g., X will be independent of field if the strain distribution is Lorentzian). For $r_c/d \gg 1$, however, the strain varies around the orbit. Watts *assumed* a Gaussian correlation relation among orbits, giving $X \propto N_d^{1/2}$ with negligible field dependence. Experimentally, the range of dislocation density suitable for dHvA measurement is $10^6 \lesssim N_d \lesssim 10^8 \text{ cm}^{-2}$. For higher densities the dHvA signals become too weak to be observable. For smaller densities the Dingle temperatures are small and comparable with the experimental error. Therefore, the experimental conditions fall near $r_c/d \approx 1$, requiring an interpolation of the Watts extremes. In his calculation the directions of the dislocations were assumed to be random and hence there is no orientational anisotropy. The dephasing of Watts and the small-angle scattering notions of TH are not necessarily incompatible. Instead, dephasing may be viewed as the physical origin of small-angle scattering.^{10,15}

Pippard¹⁶ has suggested that the existence of even one dislocation in an orbit with Bragg reflections could wipe out the contribution of this orbit to the dHvA signal. However, fairly large signals have been observed in the dog-bone orbit in copper, which has four Bragg reflections, with $N_d \approx 1.4 \times 10^7 \text{ cm}^{-2}$, which corresponds roughly to one dislocation per orbit (see Sec. IV; preliminary results appeared in Ref. 12). This indicates that Pippard's conjecture overestimates the effect of dislocations.

From a theoretical point of view, the Gaussian strain distribution assumed by Watts seems unnecessary. Instead, since both the dislocation strain field and the strain dependence of the FS in noble metals¹⁷⁻²¹ have been studied, we can carry out a first-principles calculation using a simple model of the dislocation array. Experimentally, we approach the problem by testing the field dependence of X by choosing favorable conditions over as wide a field range as possible, and exploring any anisotropic effects due to this *line* defect by measuring X for four inequivalent (111) neck orbits of one sample to eliminate sample-dependent complications. The breaking of cubic symmetry due to the linear array of edge dislocations offers a possibility to test the sensitivity of previously equivalent neck orbits to the relative orientation with respect to the dislocation line. Most measurements to be discussed have been done on the neck orbit because its X due to dislocations is large, and yet it is the orbit least sensitive to mosaic structure which often causes an apparent complication. The dHvA *relative* phase shift as

well as amplitude reduction (expressed as X) is measured, using wave-form analysis²² of dHvA signals, to extract more detailed information. For the first time we have explored both experimental measurements and theoretical calculation of the relative phase shift of the dHvA signal due to dislocations and mosaic structure. It is shown that this new parameter is a sensitive indicator of the mosaic structure of the sample and can be used to separate dislocation and mosaic-structure effects.

II. EXPERIMENTAL

From the Lifshitz and Kosevich (LK) theory^{23,24} the oscillatory magnetization associated with an extremal cross-sectional area of A of the FS in a plane normal to the applied magnetic field H is given by

$$M_r = - \sum_{r=1}^{\infty} M_r \sin[2\pi r(F/H - \gamma) \mp \pi/4], \quad (1)$$

where

$$M_r = C_r e^{-rK_0 m^* X/H}, \quad (2)$$

$$C_r = \frac{\nu T F \cos(\pi r g_c m^*/2)}{(rCH)^{1/2} \sinh(rK_0 m^* T/H)},$$

$$\nu = 2k_B (e/\hbar)^{3/2} (2\pi)^{-1/2} = 6.516 \times 10^{-6} \text{ G}^{1/2}/^\circ\text{K},$$

$$C = \left| \frac{\partial^2 A}{\partial k^2} \right|_0,$$

$$F = \hbar A/2\pi e,$$

$$K_0 = 2\pi^2 k_B m/e\hbar = 146.9 \text{ kG}/^\circ\text{K},$$

where r is the harmonic index, F is the dHvA frequency, γ is a phase constant, the \mp signs correspond to whether the extremum is a maximum or a minimum, g_c is the orbital g factor, m^* is the ratio of the cyclotron effective mass m_c to the free-electron mass m , and X is the Dingle temperature which is related to the linewidth Γ or the lifetime τ of the Landau levels through

$$X = \Gamma/\pi k_B = \hbar/2\pi k_B \tau. \quad (3)$$

A. Field-modulation technique

The field-modulation technique²⁵⁻²⁷ was used. To get strong spectrometer action the magnitude of the modulation field H_m should approximately equal the field spacing of a single oscillation. The modulation frequency ω was kept sufficiently low (54 Hz) to ensure total penetration of the modulation field into sample. The signal across a pickup coil surrounding the sample is rich in harmonics of the modulation frequency owing to the nonlinear dependence of M upon H , and is proportional to \dot{M} . This signal has the form^{24,26,27}

$$V \propto \sum_r A_r \sum_{n=1}^{\infty} n \omega J_n(\lambda_r) (\hat{M} \cdot \hat{u}) \sin(n\omega t + n\pi/2) \times \sin(\psi_r + n\pi/2), \quad (4)$$

with

$$\lambda_r = 2\pi r F H_m / H^2 = 2\pi r H_m / \Delta H, \quad (5)$$

$$\psi_r = 2\pi r (F/H - \gamma) \mp \pi/4, \quad (6)$$

and

$$\hat{M} \cdot \hat{u} = \cos\theta + \frac{1}{F} \frac{dF}{d\theta} \sin\theta,$$

where \hat{u} is the unit vector along the pickup-coil axis, θ is the angle between \hat{u} and the field direction ($\vec{M} \parallel \vec{H}$ is assumed), and $\Delta H = H^2/F$ is the field spacing of a single oscillation.

To eliminate the field dependence of the amplitude, due to $J_n(\lambda_r)$, the modulation amplitude H_m was kept proportional to H^2 , i. e., $H_m = C_m H^2$. The values of λ_r were so chosen that large dHvA harmonic content could be obtained by detecting at different harmonics $n\omega$ of the modulation frequency.

B. dHvA amplitude measurement and analysis

The dHvA measurement system was automated and it consisted of a laboratory on-line computer with input and output (I/O) devices, an interface which gave two-way communication between the computer and the experiment, magnet field generation and control, modulation-field generation, and detection of dHvA signals. (For details, see Refs. 28 and 29.)

Harmonics of the modulation frequency generated by the sample were processed with a software multichannel digital phase-sensitive detector³⁰ which was capable of detecting simultaneously two quadrature components (90° out of phase with each

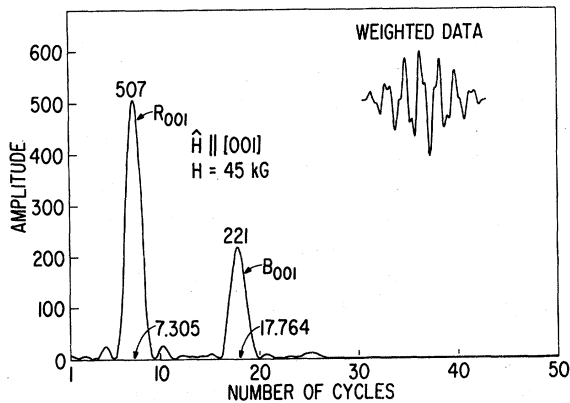


FIG. 1. Example of a Fourier transform. The data shown on the upper right corner were weighted by a triangle window function. The frequency ratio of two main oscillations is $F_{B001}/F_{R001} = 17.764/7.305 = 2.462$, and agrees very well with the accepted value.

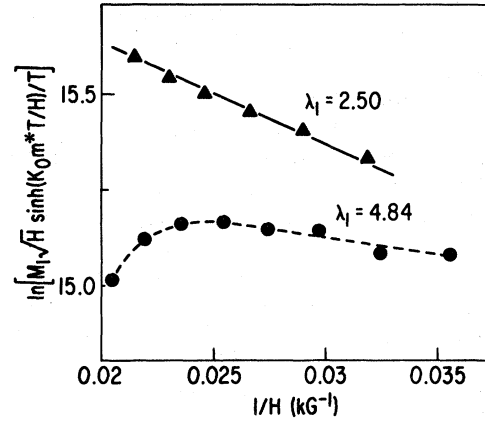


FIG. 2. Neck Dingle plots of same sample at two different λ_1 settings. Data shown in dots were taken at $\lambda_1 = 4.84$, which is very close to a Bessel zero. The amplitudes at lower field were elevated relative to those at higher field due to the skin-depth effect. This agrees with other observed Bessel plot behavior (Ref. 22). Data shown in triangles were taken at $\lambda_1 = 2.50$, which is near a Bessel maximum, and has negligible skin-depth effect.

other) of several (up to 10) even harmonics ($n\omega$ detection channels). Dingle temperatures were evaluated from the field dependence of amplitudes [Eq. (2)]. In order to avoid amplitude errors due to harmonic content and other frequency components, the amplitudes used were those resulting from an on-line Fourier analysis of a series of windows of data (each typically covering 10 to 12 dHvA cycles of the frequency of interest). An example is shown in Fig. 1. In order to recover accurate relative-phase information, it proved essential to determine amplitudes and phases in the spectrum by an iterative "Fourier decomposition" procedure (essentially a Fourier synthesis) which minimized the rms residual between data and synthesized waveform.²⁸ The ability to carry out this analysis on-line greatly facilitated the acquisition of reliable amplitudes.

Within our normal experimental field range (30–50 kG) the sample magnetoresistance saturates and the estimated skin depth was about twice the sample size. However, a more subtle skin-depth effect occurs owing to induced phase shifts,²² which modifies the Bessel function in Eq. (4), and can seriously affect precise dHvA amplitude and phase measurements. In cases where the skin depth is equal to or larger than the sample size, the amplitude of the Bessel function is modified only slightly. However, there is a shift in the position of the Bessel zeros, which is sometime substantial and also field dependent. This can lead to serious amplitude errors in Fourier components whose modulation argument λ_r [see Eq. (4)] is near such a zero. To demonstrate this effect, two Dingle

plots ($\ln M$ vs $1/H$) of the same sample taken under identical conditions except at different λ_r settings are shown in Fig. 2.

The magnetic-interaction (MI) effect³¹ is negligible in the present study. The principal effect of the MI is to change the harmonic content and hence distort the waveform. Under conditions of a weak MI the effect on the fundamental amplitude is negligible (compared to M_1). However, the lowest-order MI contribution to the second dHvA harmonic ($r=2$) may be of the same order as M_2 and is $M_2^{\text{MI}} = \frac{1}{2}\kappa M_1^2$, where $\kappa = 8\pi^2 F/H^2$. An estimate of the ratio M_2^{MI}/M_2 using known physical constants for the neck orbit in copper gives a value less than 2% (regardless of X) under typical experimental conditions. The amount of change in the measurable relative phase shift, $2\theta_1 - \theta_2$, is $\tan^{-1}[M_2^{\text{MI}} \sin 135^\circ / (M_2 - M_2^{\text{MI}} \sin 135^\circ)]$ and yields 0.83° , which is comparable to the experimental error.

C. Large-angle rotator

Since the density and distribution of the defects and mosaic structure were usually different from region to region within a crystal, a comparison among the results of different orbits from different samples is undesirable. Therefore a large-angle rotator which could observe different symmetry directions of *one* sample was constructed for the study of orbital anisotropy.³² Note that the deformation discussed later is anisotropic and breaks the cubic symmetry of the crystal.

D. Crystal growth

Careful characterizing and controlling of imperfections in sample crystals are essential in the present study. Earlier measurements¹⁰ were made on crystals from commercial sources. The characteristics of the crystals were different from one another. In general they had low as-grown residual-resistance ratios (RRR), and many subboundaries, with dislocation densities of 10^5 cm^{-2} and up. Although an oxygen-anneal treatment might increase the RRR,³³ it was found³⁴ that this treatment created dislocation clusters which yielded a background X of $\sim 0.2^\circ \text{K}$, a factor of 20 *larger* than an estimate from resistivity. Subboundaries are a source of dephasing error, and in addition are effective in blocking dislocation motion. More dislocations are formed near subboundaries during the generation of dislocations by bending, producing a nonuniform dislocation distribution. Since both impurities and imperfections limited the background in such scattering studies, it was necessary to develop in the present work techniques for the growth and preparation of very pure and nearly perfect crystals.

Prior to this work, many have reported on the

growth of copper single crystals.³⁵⁻³⁸ However, none had successfully combined both high purity and high crystal perfection.

Our goal was to grow copper single crystals of low as-grown dislocation density and high purity and yet large enough to cut a bar for bending. We employed the modified Bridgman method in which the furnace was moved relative to the crucible. The precautions taken to grow such crystals include³⁹: selecting high-purity starting material, clean crystal-growing environment, stable temperature control, and good vibration isolation. Crystals were grown in a Union Carbide Boralloy boron nitride (BN) crucible in a quartz vacuum chamber. The final crystals were 2-3 in. long and 1 in. in diameter. Vivid blaze planes could be observed on an etched⁴⁰ surface and subgrain boundaries at the surface would show up clearly. Crystals having more than one grain were given up or re-grown.

Most of the measurements to be reported were done on crystal BN5P2. Four (111) slices were cut from it and all four showed strong similarity in etch-pit pattern. Each had an as-grown dislocation density of $(2-4) \times 10^4 \text{ cm}^{-2}$ [Fig. 3(a)] and one-half of the slice was totally free from subboundaries. Some results of RRR measurements of crystal BN5P2 are listed in Table I. Since slice 1 was nearer to the last grown part of the crystal, a lower RRR value was not surprising. The oxygen annealing did not much improve the already high-purity crystals.

E. Preparation of dHvA samples with controlled dislocation densities

Crystals were cut with an acid saw and polished with an acid polishing wheel⁴¹ to minimize damage. For crystals having high dislocation densities ($> 3 \times 10^7 \text{ cm}^{-2}$) further smoothing with electrolyte polishing in phosphoric acid solution was necessary. Polished crystals were etched in Livingston etchant⁴² from 3 to 30 sec to reveal dislocation sites. Dislocation densities were determined by examination of these etched surfaces. The details of dHvA sample preparation have been described elsewhere.³⁴

To control the generation of straight edge dislocations of the same Burgers vector (single slip), pure bending has been considered to be the best method. The direction of the applied stress was so arranged that only the primary slip system might occur. Dislocations generated are mostly edge in character and the dislocation lines are parallel.⁴³ The dislocation density N_d can be controlled by properly choosing the bending radius r , since $N_d = (rb \cos \theta)^{-1}$,⁴⁴ where b is the Burgers vector and θ is the angle that the slip plane initially makes with the surface of the sample. The geom-

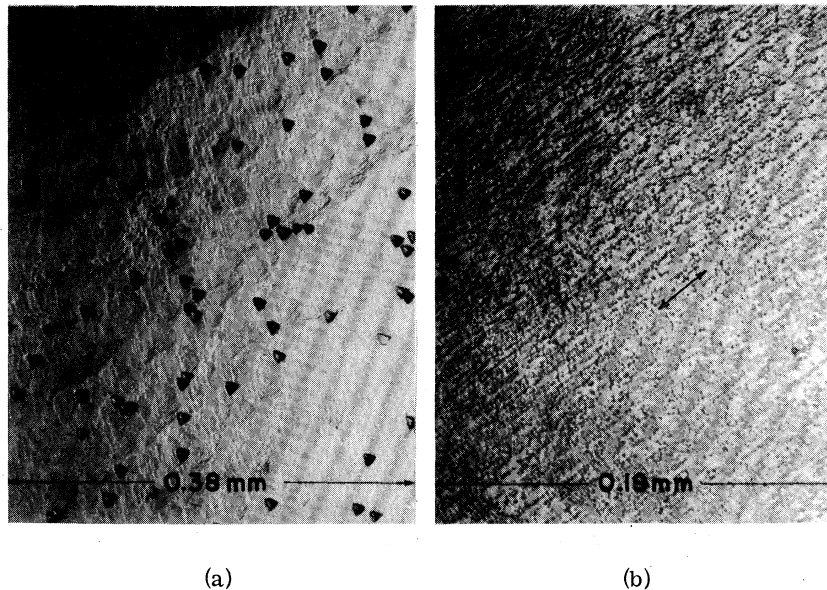


FIG. 3. Etch-pit micrographs on the (111) surface of crystal BN5P2. (a) Unstrained; $N_d \approx 3 \times 10^4 \text{ cm}^{-2}$. (b) Bent and straightened; $N_d \approx 2 \times 10^7 \text{ cm}^{-2}$. The arrow indicates the slip direction.

etry of the crystal used for bending is shown in Fig. 4. It was a rectangular bar of $3 \times 4 \times 25 \text{ mm}^3$ with faces (111), $(\bar{2}\bar{3}5)$, and $(\bar{8}71)$. The longest dimension was along $[\bar{8}71]$, which is about 7° in plane (111) from $[\bar{1}10]$ towards $[\bar{1}\bar{1}2]$. The bar was bent over a circular surface of preselected radius about the $[111]$ direction. A resolved stress analysis for this geometry predicts single slip. The bent crystal was then straightened to reduce dHvA phase cancellation due to varying orientation of each part of the crystal. Bending back would double the dislocation density. Etch pits were examined on the (111) face. The dislocation distribution of bent and straightened crystals was observed to be predominantly single slip and nearly uniform. The $(\bar{1}\bar{1}1)$ $[\bar{1}01]$ system was observed to be the primary slip system as predicted. N_d was usually higher near the edge of the crystal and decreased towards the center, probably because the dislocations were generated from the surface and moved into the bulk. Since the dHvA samples had a cross section less than $1 \times 1 \text{ mm}^2$ (and 2 mm long), it was not difficult to select a large enough region with a reasonably uniform dislocation distribution [Fig. 3(b)]. The sample dimension was smaller than that used in earlier measurements.³⁴ Though it might result in signal loss due to smaller sample mass used, it had the advantages of reducing the skin-depth effect and improving the field and defect homogeneity over the sample volume. Point defects produced during plastic deformation were annealed out while samples were prepared at temperatures between 23 and $\sim 100^\circ \text{C}$. Therefore, the main contribution to X came from dislocations which cannot be annealed out at such a low temperature.

III. THEORY

A. Some observations on the interpretation of Dingle temperatures

1. Point and slope Dingle temperatures

The Dingle temperature has been generally used as a parameter to characterize the Landau-level broadening caused by scattering and the strain field of dislocations or of other defects. The original derivation of the scattering temperature by Dingle⁴⁵ assumes a Lorentzian Landau-level line shape and a constant linewidth Γ , yielding an amplitude reduction factor for the ν th harmonic $e^{-\nu\pi(2\Gamma/h\omega_c)}$. Later work^{46,47} upgrades the formalism but does not, in essence, remove the above assumptions. If those assumptions are not valid, then the Dingle temperature determined from the logarithmic derivative of amplitudes will not be a reliable measure of scattering, and will not be related to Γ by Eq. (3). In the dislocation problem, there is a scale parameter (orbit size per dislocation spacing) and as a result we may expect a field-dependent linewidth Γ , and need not expect a Lorentzian line shape. The consequences in what can actually be measured are examined below.

TABLE I. Results of RRR measurements of crystal BN5P2.

Slice No.	Annealing condition	RRR
1	Oxygen-annealed	10 000
2	As-grown	15 000
2	Oxygen-annealed	17 000

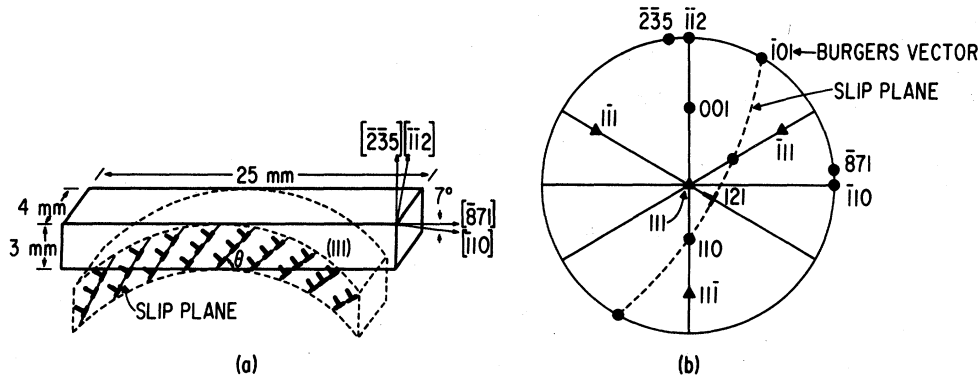


FIG. 4. Geometry of crystal bending. (a) Physical view; (b) stereographic projection.

It will be convenient operationally to retain the conventional form of the amplitude reduction factor, but to allow X a field dependence. Amplitudes will then be calculated and an $X(H)$ obtained, without the need for a specific assumption that corresponds to a line shape. The Dingle temperature described by the amplitude reduction factor is defined at a single fixed magnetic field and is called the "point" Dingle temperature to distinguish it from the conventional "slope" Dingle temperature determined from the field dependence of dHvA amplitude. Suppose we can measure the absolute dHvA amplitude M_r and denote the measured quantity as V_r (in general, V_r is a voltage); then $V_r = GM_r$, where G is the total gain of the detection system. The point Dingle temperature is then given from Eq. (2),

$$X = -(H/rK_0 m^*) \ln(V_r/GC_r). \quad (7)$$

This requires knowing the values of T , H , F , m^* , C and g_c . However, the slope Dingle temperature \bar{X} defined over a specific field range is

$$\bar{X} = -s(rK_0 m^*)^{-1} = -(rK_0 m^*)^{-1} \frac{\Delta \ln f(H, T)}{\Delta(1/H)},$$

with

$$f(H, T) = V_r H^{1/2} \sinh(rK_0 m^* T/H) / GT,$$

and s is the slope of the best least-squares-fit (LSF) straight line to the Dingle plot. Note that this does not require knowing the values of F , C , and g_c . The latter two are generally not easily available.

The connection between point and slope Dingle temperatures may be demonstrated. Let p and q be the two points where the LSF straight line intercepts the Dingle-plot curve. Then, it is found that

$$\bar{X} = X_p + Z_q(X_q - X_p)/(Z_q - Z_p), \quad (8)$$

where $Z \equiv 1/H$.

From this relation one can easily show that if

X is independent of H , the Dingle plot will be a straight line as expected [Fig. 5(a)]. However, if X is monotonically decreasing (increasing) with H , the Dingle plot will be concave downward (upward) and its slope \bar{X} will be greater (smaller) than any X value within the field range considered [Fig. 5(b)].

Note that when the field range narrows Eq. (8)

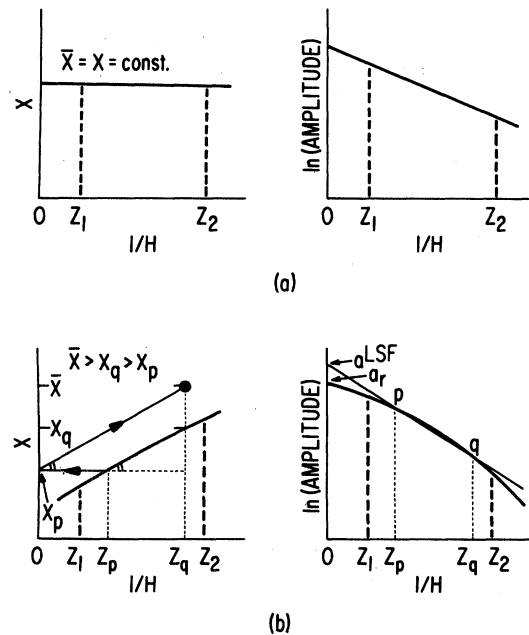


FIG. 5. Connection between the point and slope Dingle temperatures. (a) The point Dingle temperature X is independent of field H and its Dingle plot is a straight line. (b) X is monotonically decreasing with H (or increasing with $1/H$) and its Dingle plot is concave downward. The slope Dingle temperature \bar{X} can be obtained graphically by following arrows [see Eq. (8)]. Z_1 and Z_2 are limits of the field range over which the least-squares straight-line fit is made.

becomes

$$\bar{X} = X + Z \frac{\partial X}{\partial Z}.$$

The sign of $\partial X/\partial Z$ depends on the field dependence of X . This indicates that \bar{X} does not measure X even if the measurements are taken over a narrow field range.

Therefore, we conclude that only if the quantity X is independent of H will the slope Dingle temperature \bar{X} be a direct measure of X . However, if X is a function of H , then \bar{X} will depend on the field range covered and be no longer equal to X . This indicates that \bar{X} is not an accurate measure of amplitude reduction when a field dependence exists.

2. Small-angle scattering and phase smearing

The dHvA relaxation time τ differs from τ_p , that which is determined from electrical resistivity, not only in referring to a selected group of electrons on a restricted region on the FS, but also in the relative importance of small- and large-angle scattering. The scattering rate in resistivity is weighted by the factor $(1 - \cos\theta)$ in favor of larger-angle scattering.⁴⁸ By contrast, for the dHvA case, every scattering event contributes equally to the integral. The angle of scattering which suffices to destroy the phase coherence of the orbit is of order $1/n$ rad,⁹ where $n = F/H$ is the quantum number of the oscillation, and since n is typically 10^3 or 10^4 in noble metals, this angle is very small. At $H = 40$ kG in copper, this angle is 0.1° for the neck orbit and 0.004° for the belly orbit. Thus the dHvA effect is a sensitive probe for small-angle scattering.

Experimentally, earlier work¹⁰ showed a scattering rate of order 10^3 times higher as seen in the dHvA effect as compared with resistivity. This implies that small-angle scattering is dominant. We therefore focus on how to calculate that part of the scattering which is due to the long-range $1/r$ elastic strain field, and can ignore the more difficult region of the dislocation core.

Previous publications^{10,14} have discussed whether this factor of 10^3 is real or is due to amplitude reduction resulting from phase smearing in the spatially nonuniform dislocation strain field. It has been argued qualitatively¹⁰ that the two are equivalent in the present case. This agreement may be made quantitative. We borrow Pippard's result⁴⁹ for the phase change upon switching of orbit centers in magnetic breakdown, and assume it is valid for the phase change upon switching orbit centers in small-angle scattering. Pippard showed that

$$\delta\phi = \alpha\delta A_r.$$

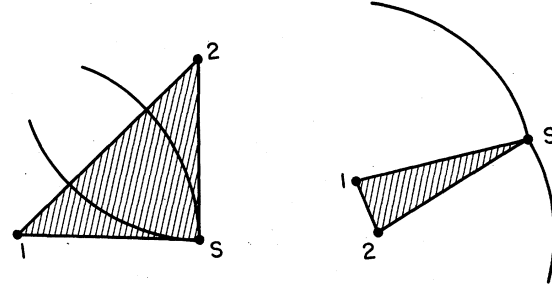


FIG. 6. Orbit-center-switching model for small-angle scattering. Left: orbit center switching upon Bragg reflection at S. The phase change on switching is the area 1S2. Right: the analogous geometry when the orbit-center switch is due to small-angle scattering at S.

Here, $\alpha = eH/\hbar c$, and δA_r is the shaded area of the triangle shown in Fig. 6 formed by the orbit centers 1 and 2 and the point of scattering S. As a check, we note that this gives the familiar criterion that the critical angle of scattering sufficient to dephase the Landau level is of order $1/n$,

$$\delta\phi = \alpha(\frac{1}{2}r^2\theta) = (\alpha/2\pi)A_r\theta = (\alpha/2\pi)(A_k/\alpha^2)\theta.$$

But

$$A_k = 2\pi\alpha(n + \gamma) \approx 2\pi\alpha n, \quad n \gg 1,$$

so that $\delta\phi = n\theta$, and the critical angle for catastrophically destructive interference is then

$$\theta_0 \gtrsim \pi/n.$$

The approach to be followed in calculating the small-angle scattering will use this equivalence to dephasing. The local phase on an orbit will be evaluated using the (assumed) local Fermi surface appropriate to the local state of strain. The net phase shift upon completion of an orbit (together with the requirement of flux quantization) will shift the eigenvalue of that orbit. A sum over inequivalent orbits will yield a net line broadening which is the desired result. Operationally, however, we calculate the contribution to M of a given orbit, and then obtain the net amplitude reduction from an average of M from different orbits. The equivalence of this to the density-of-states approach follows since M is obtained from a Fourier transform of the density of states.²³

The validity of this approach, which is essentially one of optical refraction, is presumably identical with the limits of validity of the WKB approximation. In our case, with dislocation spacings of order 10^4 Å and the de Broglie wavelength of order 10 Å, the WKB approximation is certainly valid.

B. Phase-smearing calculation

The strain field around a dislocation is planar and can be decomposed into three components:

dilation Δ (volume strain), pure shear ϵ , and pure (rigid) rotation w . In a dilational strain field the FS changes with the Brillouin-zone (BZ) size. For example, the FS of a noble metal expands with the BZ when under a hydraulic pressure.¹⁷ By contrast, a pure *shear* strain will change the *shape* of the BZ. Although the volume of the BZ remains the same, any piece of FS which is in contact with the BZ may be subject to an appreciable change. Therefore both volume and shear strain may change the dHvA phase through the change in FS. Since the volume and shear strain field around a dislocation is a long-range function of position ($1/r$), the dHvA phase ψ ($=2\pi F/H$) will vary around the electron orbit, and from orbit to orbit in a dislocated crystal. Finally, the *rotation* simply tilts the local crystal lattice and has no effect on the FS. But it can have an effect on the extremal cross section A , hence on ψ . In a crystal with an array of such defects, the strength and distribution of these components of the strain field will depend on the density and configuration of dislocations.

The phase-smearing effect of the volume and shear strain of dislocations on the dHvA signals is treated first. The effect of rotation due to dislocations is second order near symmetry directions and will be neglected in our calculation. The effect of mosaic structure in general (e.g., subgrains formed during crystal growth and latter deformation) is then treated. In both cases the Dingle temperatures and the relative phase shifts⁵⁰ are calculated in order to make direct comparison with the experimental results.

1. Dislocations

The FS extremal cross section A in momentum space varies with Δ and ϵ around a dislocation, i.e., $A=A(\Delta, \epsilon)$. The change in A due to the local variation of Δ and ϵ is

$$\delta A = \frac{\partial A}{\partial \Delta} \Delta + \frac{\partial A}{\partial \epsilon} \epsilon$$

or

$$\delta \ln A = \alpha_1 \Delta + \alpha_2 \epsilon,$$

where $\alpha_1 \equiv \partial \ln A / \partial \Delta$, and $\alpha_2 \equiv \partial \ln A / \partial \epsilon$. The notation has been chosen so that the parameters α_1 and α_2 are consistent with those used in uniaxial-stress¹⁸ and hydrostatic-pressure experiments¹⁹:

$$\delta \ln A = \alpha_1 \delta \ln A_s + \alpha_2 \epsilon.$$

Here, A_s is the extremal area of a free-electron sphere. The equivalence between Δ and $\delta \ln A_s$ follows because Δ , the volume dilation, is in fact a fractional *area* change in the two-dimensional strain field of the edge dislocation.

The dHvA phase change due to the local strain is then of the same form:

$$\delta \psi_r = 2\pi r \delta F/H = (2\pi r F/H)(\alpha_1 \Delta + \alpha_2 \epsilon). \quad (9)$$

Hence the higher dHvA harmonics are more sensitive to phase variation than the fundamental ($r=1$). Note that Δ and ϵ are functions of position (on the orbit in real space) and hence depend on the magnetic field through the change of orbit size. (The subscript 1 will be dropped whenever there is no confusion.)

The three components of the elastic strain field of an edge dislocation are:
the dilation

$$\Delta = -\frac{b(1-2\nu)}{2\pi(1-\nu)} \frac{y}{x^2+y^2}; \quad (10)$$

the pure shear

$$\epsilon = \frac{b}{4\pi(1-\nu)} \frac{x(x^2-y^2)}{(x^2+y^2)^2}; \quad (11)$$

and the pure rotation

$$w = \frac{b}{2\pi} \frac{x}{x^2+y^2}, \quad (12)$$

where ν is Poisson's ratio. We have taken the dislocation line as the z axis and its Burgers vector along the positive x axis. Note that Δ is symmetric about the y axis and antisymmetric about the x axis, but ϵ is symmetric about the x axis and antisymmetric about the y axis. This has consequence in breaking the symmetry of scattering on previous equivalent orbits.

Substituting the expressions Δ and ϵ from Eqs. (10) and (11) into Eq. (9) gives, at any point (x, y, z) in a dislocation strain field, the phase change (in radians)

$$\delta \psi(x, y) = 1.18(F/H)G(\alpha_1, \alpha_2, x, y),$$

with

$$G(\alpha_1, \alpha_2, x, y) = \frac{1}{x^2+y^2} \times \left(-\alpha_1 y + 1.667 \alpha_2 \frac{x(x^2-y^2)}{x^2+y^2} \right),$$

where both F and H are in gauss, and x and y are in angstroms. The values of $b=2.56 \text{ \AA}$ and $\nu=0.35$ for Cu were used in above derivation. We then convert the coordinates of the dislocation strain field to the coordinates on the electron orbit and obtain $\delta \psi = \delta \psi(x_0, y_0, \phi)$, where (x_0, y_0) are the coordinates of the orbit center and ϕ is the angular position of the point of interest on the orbit.

The oscillatory magnetization of a volume element dV having a phase change $\delta \psi$ is

$$M = M_0 \sin(\psi_0 + \delta \psi),$$

where $\psi_0 = 2\pi r(F/H - \gamma) \mp \pi/4$. Then the average magnetization over the sample volume V_s is given

by

$$\bar{M} = \frac{1}{V_s} \int_{V_s} M_0 \sin(\psi_0 + \langle \delta\psi \rangle) dV, \quad (13)$$

where $\langle \delta\psi \rangle$ is the averaged phase change over a given orbit,

$$\langle \delta\psi \rangle = \frac{1}{2\pi} \int_0^{2\pi} \delta\psi(x_0, y_0, \phi) d\phi. \quad (14)$$

Here we have assumed that the phase changes around an orbit are *coherent* so the averaged phase change $\langle \delta\psi \rangle$ is the sum around the orbit. This assumption appears valid since we are in the domain in which the WKB approximation is valid. Since the strain field around a dislocation is planar, Eq. (13) may be rewritten

$$\bar{M} = M_0 (C \sin\psi_0 + S \cos\psi_0),$$

with

$$S = \frac{1}{A_0} \int_{y_{01}}^{y_{02}} \int_{x_{01}}^{x_{02}} \sin(\langle \delta\psi \rangle) dx_0 dy_0, \quad (15a)$$

$$C = \frac{1}{A_0} \int_{y_{01}}^{y_{02}} \int_{x_{01}}^{x_{02}} \cos(\langle \delta\psi \rangle) dx_0 dy_0, \quad (15b)$$

where A_0 is the area of a domain bounded by x_{01} , x_{02} , y_{01} , and y_{02} . The choice of the domain A_0 will be discussed later.

Let

$$S = A_d \sin\delta_d, \quad (16a)$$

$$C = A_d \cos\delta_d; \quad (16b)$$

then

$$A_d = (S^2 + C^2)^{1/2}, \quad (17a)$$

$$\delta_d = \tan^{-1}(S/C), \quad (17b)$$

and the averaged magnetization becomes

$$\bar{M} = M_0 A_d \sin(\psi_0 + \delta_d). \quad (18)$$

The quantity A_d is the amplitude-reduction factor due to phase smearing and is smaller than 1; δ_d is the resultant phase shift.

So far we have only considered the strain field produced by a single dislocation. In principle, the dislocation strain field at a given point in a dislocated crystal is the superposition of all strain fields produced by all dislocations. Although the strain field is long range ($1/r$), it has both signs in the case of edge dislocations. We may assume that the distribution of distant dislocations is random and the superposition of their strains at the point of interest vanishes. Therefore, we adopt a model in which only nearby dislocations are taken into account. In this model all dislocations are assumed parallel (to [121]) and formed along slip lines. (This assumption is fairly well justified experimentally.) The geometry of the dislocation

configuration in this model is shown in Fig. 7. The parameter ξ is the ratio of the dislocation spacing between slip lines to the spacing d in a slip line. The value of ξ is of the order of 1–5 from experimental observation. The dislocation density N_d , counted on the (111) face, is then $N_d = \cos\theta_0 / (\xi d^2)$, where $\theta_0 = 19.47^\circ$ is the angle between the average dislocation line [121] and [111], the normal to the actual plane of observation. Thus, the dislocation spacing in a slip line is $d = 0.971(\xi N_d)^{-1/2}$. For a density $N_d = 2 \times 10^7 \text{ cm}^{-2}$, the spacing d ranges from 21600 Å ($\xi = 1$) to 9700 Å ($\xi = 5$).

The periodicity of the dislocation configuration in this model makes it natural to choose the integration domain A_0 of orbit centers (x_0, y_0) as the shaded area shown in Fig. 7. Finally, Eq. (15) becomes

$$S = \frac{N_d}{\cos\theta_0} \times \int_{-td/2}^{td/2} \int_{-d/2}^{d/2} \sin\left(\frac{1}{2\pi} \int_0^{2\pi} \delta\psi(x_0, y_0, \phi) d\phi\right) dx_0 dy_0, \quad (19a)$$

$$C = \frac{N_d}{\cos\theta_0} \times \int_{-td/2}^{td/2} \int_{-d/2}^{d/2} \cos\left(\frac{1}{2\pi} \int_0^{2\pi} \delta\psi(x_0, y_0, \phi) d\phi\right) dx_0 dy_0. \quad (19b)$$

Trial calculations on the strain field produced by various numbers of dislocations indicate that the strain field produced by dislocations outside the central nine (3×3) dislocations has a negligible effect, except at low magnetic field (say, $< 20 \text{ kG}$),

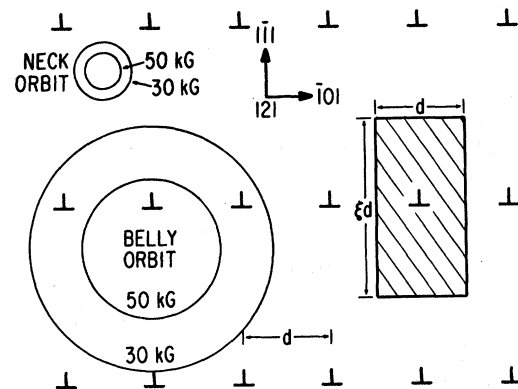


FIG. 7. Dislocation configuration used in the phase-smearing calculation. Dislocations are lined up along slip lines with lowest-energy configuration (polygonization). The shaded area indicates the integration domain of an orbit center. Both neck and belly orbits are sketched for appropriate field limits used in the experiment and they are plotted in the plane normal to dislocations for convenience. In this example, N_d is 10^7 cm^{-2} and ξ is 2.

where more dislocations ($> 5 \times 5$) were included. This justifies the negligible influence of distant dislocations.

The mathematical formula for the dislocation strain diverges near the dislocation core. The divergence is avoided by choosing a proper cutoff radius r_0 . The strain within the core region is assumed to be the same as the strain at $r = r_0$. In the actual calculation the core radius was chosen to be 10 Å. Ignoring the core is justified by the overwhelming dominance of the long-range $1/r$ strain field on the dephasing discussed earlier. The calculated results were indeed found to be insensitive to the choice of r_0 .

There are two main steps in the calculation: the orbital averaging and then the sample averaging. To get some physical insight about how the integration sums up the contributions from various parts of the strain field, we define two quantities $S(y)$ and $C(y)$ from Eq. (19),

$$S(y) = \frac{N_d}{\cos \theta_0} \int_{-\xi d/2}^y \int_{-d/2}^{d/2} \sin \left(\frac{1}{2\pi} \int_0^{2\pi} \delta\psi(x_0, y_0, \phi) d\phi \right) \times dx_0 dy_0,$$

$$C(y) = \frac{N_d}{\cos \theta_0} \int_{-\xi d/2}^y \int_{-d/2}^{d/2} \cos \left(\frac{1}{2\pi} \int_0^{2\pi} \delta\psi(x_0, y_0, \phi) d\phi \right) \times dx_0 dy_0,$$

where we have replaced the upper limit of the integration of y_0 by a variable quantity

$$y = (\xi d/N_y) n_y - \xi d/2, \quad n_y = 1, 2, 3, \dots, N_y.$$

The integration domain is divided into N_ϕ , N_x , and N_y intervals along ϕ , x_0 , and y_0 coordinates, respectively. Hence the quantity $S(n_y)$ is the accumulated sine-part contribution to the amplitude A_d from the $n_y + 1$ rows of orbits (each row has $N_x + 1$ orbits whose centers are aligned along the x direction). Similarly, $C(n_y)$ is the accumulated cosine-part contribution to A_d . Note that $S(N_y) = S$, and $C(N_y) = C$. The quantities $S(n_y)$ and $C(n_y)$ vs n_y for two different sets of parameters are shown in Fig. 8. Some general features can be seen from those curves. First, the quantity $S(n_y)$ is symmetric about $n_y = N_y/2$ and the final integral S vanishes because $S(n_y)$ is an odd function of an antisymmetric strain field. *This results in a zero value for the dHvA phase shift δ_d , defined in Eq. (17b).* Second, when the phase change $\delta\psi_r$ is small, $C(n_y)$ increases smoothly with n_y . However, when $\delta\psi_r$ becomes large, the contributions from certain rows of orbits may change sign and become destructive interference.

The point Dingle temperature is calculated by equating the amplitude reduction factor A_d to the

Dingle factor,

$$X = - (H/K_0 m^*) \ln A_d.$$

To obtain the slope Dingle temperature \bar{X} , values of A_d are calculated at a set of selected field values (e.g., field values used in experimental measurements). Then \bar{X} is determined from the slope of the LSF of a straight line to the $\ln A_d$ -vs- $1/H$ plot.

Although the results of calculation depend on many parameters, the main features of the calculated Dingle temperature X as a function of field have the general form shown by the examples in Fig. 9. For a given set of parameters a divergence occurs in X at a certain magnetic field H_c . The position of this divergence depends on the magnitude of the phase change $\delta\psi_r$, given by Eq. (9), and on the integration domain A_0 (i.e., N_d and ξ). For example, the divergence moves toward the high-field end when $\delta\psi_r$ becomes larger. The over-all curve rises when H_c becomes larger. The width of the divergence when plotted vs $1/H$ is approximately constant. The divergence in X is equivalent to a vanishing amplitude in M and is a consequence of the perfect periodicity of the model used in the calculation together with the antisymmetry of the strain field surrounding an edge dislocation. The divergence occurs when the orbit size is comparable to the dislocation spacing. Near the field H_c large cancellation among contributions from different orbits at different locations occurs and results in a vanishing amplitude. In a real crystal this periodicity does not strictly hold, and hence a strong smearing of the divergence results. Although the slip-line model overestimates the effect, we expect the general structure of $X(H)$ to be retained, with the following consequences. Since the Dingle temperature is field dependent, the Dingle plot has curvature. The Dingle temperature increases with the field on the low-field wing and decreases on the high-field wing of an $X(H)$ curve. It has a weak field dependence at the high-field end. It also increases with the dislocation density N_d according to the relation $X \propto N_d^n$, where the value of n depends on H and other parameters. At the high-field limit, the value of n lies between $\frac{1}{2}$ and 1.

The observed behavior of X depends on the magnetic field "aperture" actually taken during measurements. For example, the conditions of all our experimental measurements of the neck oscillation fundamental (M_1) fell on the high-field wing of an $X(H)$ curve. However, the conditions of measurements of the second-harmonic neck oscillations fell on the low-field wing of a *different* curve, with a larger H_c (see Fig. 9). In general, the second-harmonic Dingle temperature X_2 is larger than the first-harmonic Dingle temperature X_1 .

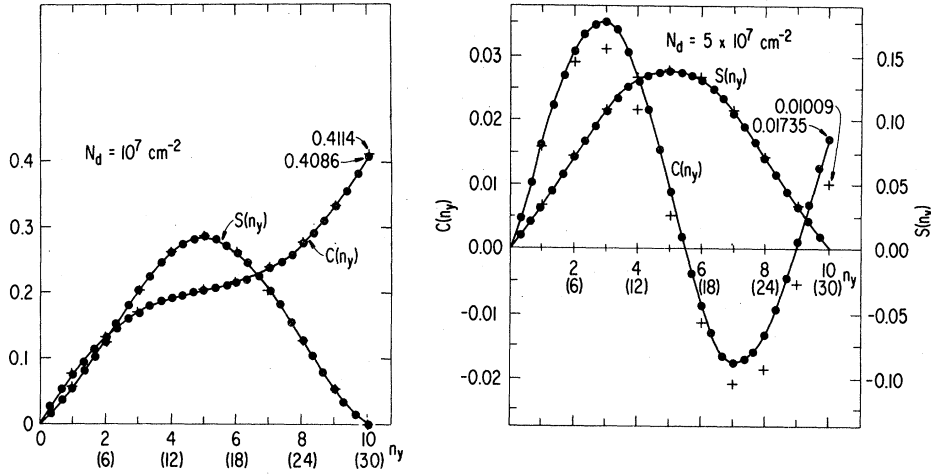


FIG. 8. Plots of $S(n_y)$ and $C(n_y)$ vs n_y for two dislocation densities at $H=30$ kG with $\alpha_1=15$, $\alpha_2=-16$, $\xi=2$, and a 3×3 dislocation array. +, low density of divisions: $N_x \times N_y = 10 \times 10 \times 10$. ●, high density of divisions: $N_x \times N_y = 60 \times 30 \times 30$. The scale of n_y , shown in parentheses is for the higher density of divisions. The error in X while using the lower density of divisions is 0.7% for $N_d=10^7$ cm^{-2} and 13.4% for $N_d=5 \times 10^7$ cm^{-2} .

2. Mosaic structure

The average magnetization over a spread of misoriented crystallites (subgrains) in a sample is

$$\bar{M} = M_0 \langle \sin(\psi_0 + \delta\psi) \rangle,$$

where the average is taken over the quantity $\sin(\psi_0 + \delta\psi)$. There is no phase change around an orbit within each crystallite. By contrast, in a dislocation strain field the phase varies around the orbit.

The amplitude reduction factor (Dingle temperature) of a crystal with mosaic structure has been reported earlier.^{31,51} However, the relative phase shift is a new result,³⁹ and offers a way to distinguish between several otherwise indistinguishable phase-smearing mechanisms. We find that the relative phase shift due to mosaic structure has a strong field and angular dependence, in contrast to that due to dislocations. Two cases will be discussed: a bicrystal made of two equal crystals inclined at an angle β , and a Gaussian spread of misorientations with a characteristic halfwidth β . In each case the mean symmetry axis is tilted at an angle θ_0 from the magnetic field H .

In the case of a bicrystal the amplitude reduction factor is

$$A_m = \cos\left(\frac{\pi F'(\theta_0)\beta}{H}\right) \approx \cos\left(\frac{\pi F''(\theta_0)\beta}{H}\right), \quad (20)$$

for small θ_0 , and the phase shift

$$\delta = \frac{\pi F''(\theta_0)}{H} \frac{\beta^2}{4},$$

and then the relative phase shift

$$2\delta_1 - \delta_2 = 0. \quad (21)$$

At a fixed magnetic field beats may be observed in a rotation curve. The number of beats is proportional to F'' , β , and $1/H$. If the two crystals are not equal in volume, then the beat zeros become

minima. At a sufficiently large tilt beats may be seen in the Dingle plot. The number of beats within a given field range is proportional to F'' , θ_0 , and β . For a given sample the beats are more easily seen in the second-harmonic Dingle plot than in the first-harmonic Dingle plot. Such a structure was seen in the course of this experiment, with a beat in M_2 yet no beat in M_1 .

In the case of Gaussian spread of misorientation the amplitude reduction factor is

$$A_m = \frac{1}{(1+\gamma^2)^{1/2}} \exp\left(-\frac{\theta_0^2 \gamma_a^2}{\beta^2(1+\gamma^2)}\right), \quad (22)$$

and the phase shift

$$\delta = \tan^{-1}\gamma - \frac{\theta_0^2 \gamma_a^2 \gamma}{\beta^2(1+\gamma^2)},$$

with $\gamma = t\beta^2$ and $\gamma_a \theta_0 = \frac{1}{2} a\beta^2$, where $a = 2\pi F'(\theta_0)/H$

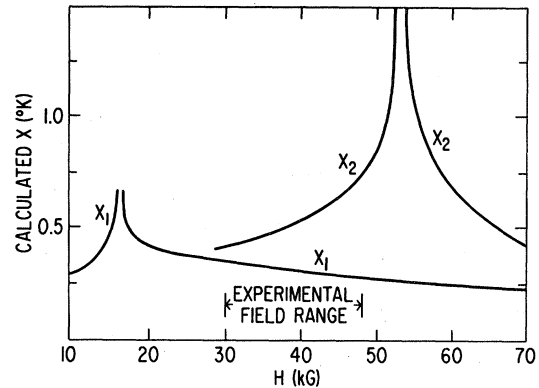


FIG. 9. Example of calculated $X(H)$ vs H for a $N_d = 1.5 \times 10^7$ cm^{-2} . Parameters used in the calculation are $\alpha_1=15$, $\alpha_2=-16$, $\xi=2$, and a 3×3 dislocation array for $H \geq 29$ kG and a 5×5 dislocation array for $H < 29$ kG. X_1 and X_2 are fundamental and second-harmonic Dingle temperatures, respectively.

TABLE II. Summary of calculated phase-smearing results.

(a) Amplitude reduction [the measurable quantity (parameter) is the Dingle temperature]:		
	Dislocations	Mosaic structure
At symmetry	dominating	negligible
Off symmetry	insensitive to tilt	increases quickly with tilt
(b) Relative phase shift (measured as $2\theta_1 - \theta_2$):		
	Dislocations	Mosaic structure
At symmetry	0°	$\sim 0^\circ$
Off symmetry	0°	increases quickly with tilt, strong field dependence

and $t = \pi F''(\theta_0)/H$, and then the relative phase shift

$$2\delta_1 - \delta_2 = \tan^{-1} \left(\frac{2\gamma^3}{1+3\gamma^2} + \frac{6\theta_0^2 \gamma_a^2 \gamma}{\beta^2(1+\gamma^2)(1+4\gamma^2)} \right) \quad (23)$$

If the angular dependence of F near the symmetry direction is parabolic, then $a \approx 2t\theta_0$ and $\gamma_a \approx \gamma$. Note that it is the second-order term in the expansion of F ($t \neq 0$) that leads to the nonvanishing relative phase shift. Some interesting results can be derived from Eqs. (22) and (23). The Dingle temperature X depends on both H and θ_0 . At a given tilt X decreases with H . It has a minimum at the symmetry direction ($\theta_0 = 0$) and increases with the tilt quickly (nearly $\propto \theta_0^2$). The above phenomena are stronger in orbits with large F'' . However, measurements on those orbits are more difficult because the amplitude damps out quickly as tilt goes up.

The most striking result is that the relative phase shift has a strong field and angular dependence. This can be used to separate the effect of mosaic structure from that of dislocations, which have a zero relative phase shift. A summary of calculated phase-smearing results is presented in Table II.

IV. EXPERIMENTAL RESULTS

The effect of dislocations can be studied with dHvA measurements made with H along a symmetry axis, where the influence of the mosaic structure is negligibly small. On the other hand, the effect of mosaic structure can be studied with measurements made with the sample tilted away from the symmetry axis, because the effect of dislocations is insensitive to the tilt. Therefore, although dislocations and mosaic structure coexist in the same sample, it is possible to separate their influences.

Two copper single crystals were used in the present measurements. One was a commercial

crystal which had an O_2 -annealed RRR of 2500 and an as-grown $N_d \approx 5 \times 10^5 \text{ cm}^{-2}$. (This crystal was called RCI 812.) One bar was cut from it and deformed and had a $N_d = (1.4 \pm 0.1) \times 10^7 \text{ cm}^{-2}$. Most results came from crystal BN5P2, grown by us. Five bars were cut from it and deformed. Several dHvA samples were prepared from these strained as well as unstrained crystals. All slope Dingle temperatures \bar{X} given later were determined from the fundamental dHvA amplitudes of the 2ω detection channel. The values of effective masses were taken from Halse.⁵²

A. Dislocations

1. Amplitude reduction

The anisotropic effect due to the presence of line defects was investigated by measuring \bar{X} of four inequivalent $\langle 111 \rangle$ neck orbits ($N_{\langle 111 \rangle}$) of the same sample (BN5P2-4), which had a $N_d \approx (1.1 \pm 0.2) \times 10^7 \text{ cm}^{-2}$. These results are given in the second column of Table III. The errors given in the table were derived from the standard deviations of the slopes of Dingle plots plus an uncertainty of $\pm 0.02^\circ \text{K}$ in the temperature measurement. An anisotropy was observed, with the $[1\bar{1}1]$ neck orbit ($N_{[1\bar{1}1]}$) whose plane is normal to the plane of the dislocation strain field having the largest \bar{X} (and hence largest amplitude reduction), and the $[111]$ neck orbit ($N_{[111]}$) whose plane is nearly parallel to the plane of the dislocation strain field having the smallest \bar{X} . These measured \bar{X} are normalized to that of $N_{[1\bar{1}1]}$ and are shown in the third column. The same ratios from our dephasing calculations are shown in the fourth column. The agreement between the observed and calculated anisotropy is good.

At first it seems that the $N_{[111]}$ senses the largest phase variation around the orbit and would be expected to have the largest Dingle temperature. However, its *averaged* phase change around an orbit is less because of the odd symmetry of the dislocation strain field. Thus, the averaged phase changes of orbits from *different* regions of the sample have less variation than those of $N_{[1\bar{1}1]}$ and hence less destructive interference among orbits.

TABLE III. Comparison of observed and calculated four $\langle 111 \rangle$ neck slope Dingle temperatures. Parameters used in the calculation are $\alpha_1 = 15$, $\alpha_2 = -16$, $\xi = 2$, and a 3×5 dislocation array.

Field direction	\bar{X}^{obs}	$[\bar{X}/\bar{X}([1\bar{1}1])]^{\text{obs}}$	$[\bar{X}/\bar{X}([1\bar{1}1])]^{\text{calc}}$
$[111]$	0.35 ± 0.04	0.44 ± 0.09	0.55
$[\bar{1}11]$	0.47 ± 0.04	0.59 ± 0.08	0.58
$[11\bar{1}]$	0.60 ± 0.07	0.76 ± 0.15	0.65
$[1\bar{1}\bar{1}]$	0.79 ± 0.06	1.00	1.00

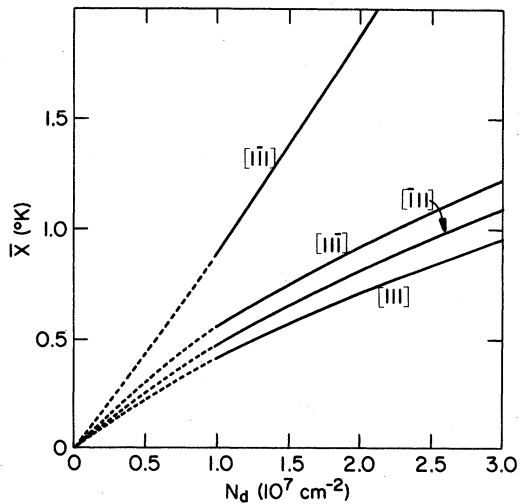


FIG. 10. Calculated \bar{X} (over 33 to 48 kG) of four neck orbits as a function of N_d . Same set of parameters are used as in Fig. 9 but with a 3×5 dislocation array.

Note that although the symmetry of Fig. 4 would require $X(\bar{1}11) = X(1\bar{1}\bar{1})$ in a dilational strain field alone, this symmetry is destroyed by the shear component which is also included in the calculation. Owing to the specific geometry used in the present experiment the $[\bar{1}\bar{1}\bar{1}]$ direction might have the largest spread of subgrain tilt resulting from possible wobbling of the slip planes. However, this would not affect our measured results because these data were taken with (111) directions well aligned to field direction.

The calculated slope Dingle temperature \bar{X} of $\langle 111 \rangle$ neck orbits as a function of N_d are shown in Fig. 10. Note that in addition to the anisotropy already mentioned (Table III) there is a difference in dependence on N_d , ranging from nearly linear ($[\bar{1}\bar{1}\bar{1}]$) to a pronounced concave-downward curvature ($[111]$). However, over the *experimentally accessible range* (solid curves), all four are nearly linear. This differs from the results of Watts,¹⁴ predicting a dependence proportional to $N_d^{1/2}$ in the limit $r_c/d \gg 1$ (high N_d or low H). Four neck anisotropy ratio is rather insensitive to the precise dislocation density and is not consequence of the precise periodic array.

The measured \bar{X} of various orbits are shown in Fig. 11 as a function of N_d . The data from other sources^{10,13} are also included. Note that the TH data¹⁰ were also measured on samples with a well-defined linear dislocation array generated by pure bending. However, the CW data¹³ were measured on samples with randomly oriented dislocations generated either by squeezing the sample in a micrometer or by spark cutting the sample on a coarse range, so it is not surprising that their \bar{X}

values are quite different from ours. Our results for the $[111]$ neck orbit can be fitted well to a straight line. (Other orbits seem to follow the same trend but there are not enough data to make a strong statement.) This agrees with earlier measurements made by TH. We note that the TH results are on samples of about a factor-of-10-less purity, with a consequent 0.2°K uncertainty in the "background" \bar{X} which is absent in the present results (especially for the neck, which is least sensitive to mosaic structure). Note that the present neck results have a larger slope (dotted line) than TH (dashed line), presumably because both the purity and perfection of the crystals used in this study were better, and hence less dislocation clustering occurs during deformation. The experimental results are in surprising semiquantitative agreement with the first-principles (Fig. 10, $[111]$) calculation. The agreement could be made perfect by a parameter adjustment, which we do not view as physically significant (see Sec. V). Note also there is no evidence for significant curvature in our experimental regime of the sort predicted by Watts.

Our efforts to measure the ratios $\bar{X}_N/\bar{X}_N(1\bar{1}\bar{1})$ as a function of N_d for comparison with Fig. 10 were not successful, because of the difficulty in orienting the symmetry directions *other* than $[111]$ in the more highly dislocated samples. The dHvA signals were much weaker because of the large pickup coil tilt (70.5°) and to a probable larger content of mosaic structure introduced into such samples while generating dislocations at high N_d .

The anisotropy of \bar{X} among different orbits is also apparent, with the D_{110} having the largest \bar{X} followed by R_{001} , N_{111} , B_{111} , and B_{001} in that order. Especially, \bar{X} of D_{110} , R_{001} , and N_{111} tend to form

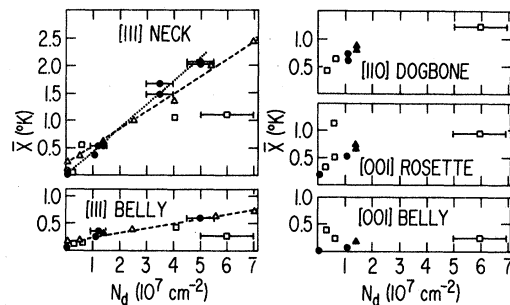


FIG. 11. Experimental slope Dingle temperature \bar{X} as a function of sample dislocation density N_d . The uncertainty in N_d is typically 10%. Large uncertainties are shown with error bars. The uncertainty in \bar{X} is typically less than 0.1°K . Our results are shown in solid circles (crystal BN5P2) and triangles (crystal RCI 812). Terwilliger and Higgins, Ref. 10 (open triangle) and Coleridge and Watts, Ref. 14 (open square) results are also shown.

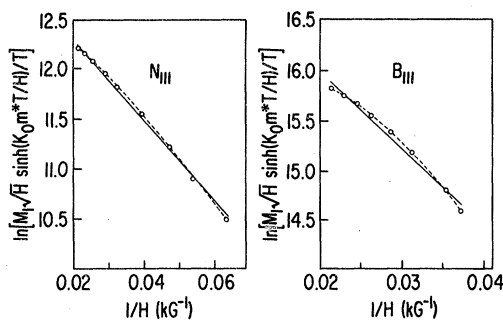


FIG. 12. [111] neck and belly Dingle plots of sample RCI 812-3.

a group which has large X , and the two bellies form another group which has smaller \bar{X} . The CW results show some similarity, but their values are much lower at higher N_d , which could be attributed to the random directions of dislocations as well as to the nonuniformity of dislocation distribution in their samples. Note also that the belly orbits, which are *most* sensitive to mosaic structure, have the smallest \bar{X} . This is more evidence that the effect of mosaic structure is minimized at a symmetry direction. The fact that the \bar{X} of the dog-bone, rosette, and neck orbits are larger is because these orbits are in contact with the BZ boundary, and hence have larger fractional changes in FS cross sections under strain than bellies which are not. Therefore, they experience larger variations in dHvA phase than the bellies and suffer larger amplitude reduction.

Our calculation predicts a field-dependent X that decreases with H , which would produce a small (concave downward) curvature in the Dingle plot. [Figure 9, $X_1(H)$ corresponds to case (b) of Fig. 5.] However, this curvature is usually buried in the experimental error in the amplitude measurements when only a limited field range is taken. In order to detect such a curvature of wide field range has to be covered so that the curvature will be sizable and yet still be certain to minimize the MI and skin-depth effects which may lead to a spurious curvature. We have been able to fulfill all these requirements in sample RCI 812-3. Because of its lower value of RRR (~ 2500) we were able to use a larger sample and a higher modulation frequency (100 Hz), resulting in a detectable dHvA N_{111} signal over a range of $1/H$ triple that used in most of the measurements. The Dingle plots of N_{111} and B_{111} orbits obtained from this sample are shown in Fig. 12. The results display obvious curvature, a positive indication that the Dingle temperature due to dislocations is field dependent, with the sign of dX/dH predicted by the phase-smearing calculations (Fig. 9) for the neck.

However, a field-dependent Dingle temperature

gives a small effect (the curvature in the Dingle plot), and the usual \bar{X} is not a good indicator of $X(H)$. A useful measure of the point X may be obtained from the harmonic ratio M_2/M_1 at a single H .²² In the simplest situations

$$\frac{M_2}{M_1} \propto \frac{e^{-2K_0 m^* x/H}}{e^{-K_0 m^* x/H}} = e^{-K_0 m^* x/H}. \quad (24)$$

Therefore $\ln(M_2/M_1)$ at a single H value can yield $X(H)$. The results measured on N_{111} of sample BN5P2-4 [whose measured $\bar{X}(111) = 0.35 \pm 0.04$ °K] are shown in Fig. 13 (X^0). Also shown (X_1) are the results of the phase-smearing calculation which would yield the observed \bar{X} . Note that the X^0 are about a factor of 2 larger than \bar{X} , demonstrating that very substantially different measures of scattering can come out of the same experimental data. The results indicate not only that X^0 and X_1 have an opposite field dependence but also that X^0 is much larger than X_1 . This contradiction was caused by assuming $X_2 = X_1$ in deriving Eq. (24). In general, $X_2 \neq X_1$ and the measured quantity X^0 is actually $X_{21} = 2X_2 - X_1 = (2p - 1)X_1$, where p is the ratio X_2/X_1 and is in general field dependent. The fact that $X^0 > X_1$ is consistent with our calculation (Fig. 9), which gives $p > 1$ for the field range under consideration and hence $X_{21} > X_1$. The observation that X^0 is increasing with H is related to the fact that X_2 increases with H and $X_2 > X_1$ in the field range under consideration. Since the experimental field range is away from the (overestimated) divergence of calculated X_1 , contrary to X_2 (see Fig. 9), we feel that the calculated values of X_1 are more reliable than the X_2 values. We then use the calculated X_1 to estimate X_2 from X^0

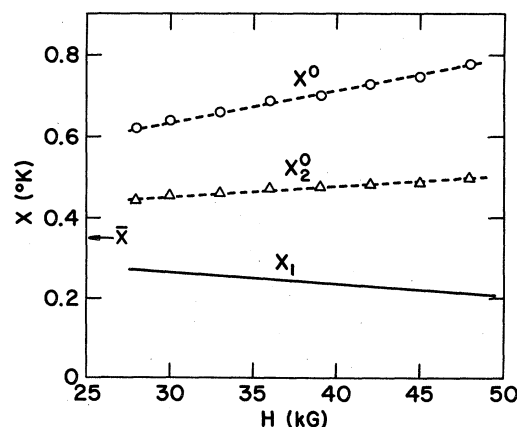


FIG. 13. Comparison of experimental field-dependent X values [X^0 , obtained from harmonic ratio M_2/M_1 as in Eq. (24)] and values (X_1) calculated by phase smearing. The calculated values have been adjusted to a given a slope \bar{X} of 0.35 °K, equal to that observed in this crystal. Values of X_2^0 are obtained from the relation $X_2^0 = (X^0 + X_1)/2$.

and X_1 by the relation $X_2^0 = (X^0 + X_1)/2$. These results are shown as triangles in Fig. 13. We find that X_2^0 is greater than X_1 and increases with H . Both the relative size and the sign of the slope are consistent with the theoretical results for X_2 shown in Fig. 9, but the smaller magnitude of the slope indicates a strong smearing of the divergence in a real crystal.

These results have demonstrated that (a) the Dingle temperatures due to dislocations are field dependent, (b) the second-harmonic Dingle temperature X_2 may not be equal to the first-harmonic Dingle temperature X_1 , and in such a case Eq. (24) will not hold, and (c) the traditional slope Dingle temperature \bar{X} does not directly measure the true Dingle temperature X when X is field dependent. Although above conclusions are obtained from a dislocation problem, it has strong implications of being applicable to the general scattering problem, especially when the Dingle temperature has a field dependence.

2. Relative phase shift

Our dephasing calculation predicts no relative phase shift, because the contribution to the sine part cancels exactly, owing to the antisymmetric strain field produced by the dislocation. This is unambiguously confirmed by our experimental results (e.g., see Fig. 16, for $\theta_0 = 0$) which give a shift from the LK value of $0.0^\circ \pm 1^\circ$.

B. Mosaic structure

Although mosaic structure can be reduced to a minimum with very careful crystal growth and sample treatment, sometimes it is unavoidable. It is then important to be able to separate it from other

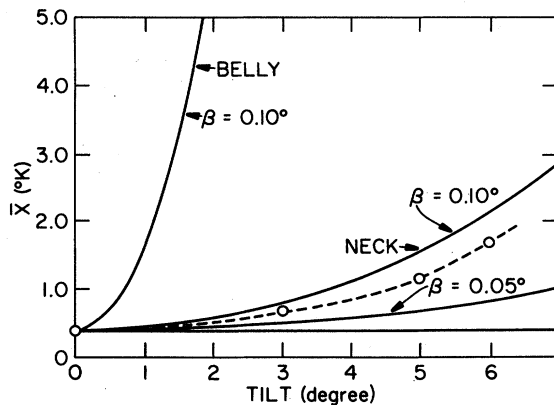


FIG. 14. Effect of mosaic structure on the neck orbit. Data are shown in circles. Calculated results (over 33 to 48 kG) are shown as solid curves. The horizontal line is the \bar{X} due to a dislocation effect measured at [111]. For comparison, a calculation of the (much larger) effect on the belly orbit is also shown.

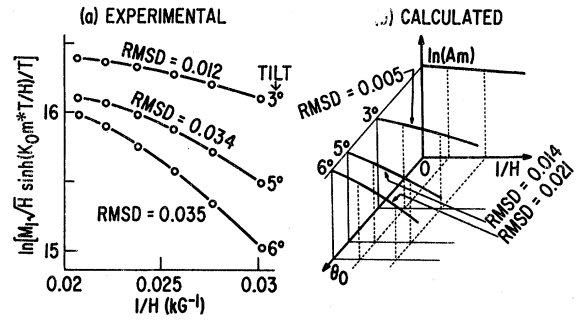


FIG. 15. Curvatures in neck off-symmetry Dingle plots. (a) Experimental Dingle plots at tilts of 3° , 5° , and 6° from [111]; (b) calculated curves shown over same field range.

effects under investigation. We have studied the effect of mosaic structure by doing measurements at off-symmetry directions. The measured results were compared with the calculation based on a Gaussian spread of misorientations of half-width β . The value of β of the sample has been estimated from several independent measurements. (Note that the value of β we determine depends upon the plane of rotation of H because the deformation we performed was anisotropic.)

1. Amplitude reduction

The measured slope Dingle temperature \bar{X} of the [111] neck orbit of sample BN5P2-4 as a function of tilt θ_0 is shown in Fig. 14. The calculated \bar{X} [from Eq. (22)] using $\beta = 0.05^\circ$ and 0.1° are also shown. The horizontal line is the background Dingle temperature due to dislocations measured at the symmetry direction. By comparing the measured results with the calculated curves we find $\beta = 0.08^\circ \pm 0.01^\circ$. This value is smaller than other estimates to be described later. This is probably because at off-symmetry directions the Dingle plots had curvatures (Fig. 15), which caused an underestimation of \bar{X} . However, these results indicate that the effect of mosaic structure is minimum at the symmetry direction and the Dingle temperature increases very quickly with tilt nearly as θ_0^2 . This supports the assumed Gaussian spread of misorientations in this sample.

Even with a relative small mosaic structure, the effect of \bar{X} away from a symmetry direction may be large. The calculated \bar{X} for <111> belly with $\beta = 0.1^\circ$ is also shown in Fig. 14 to demonstrate that the effect of even a small amount of mosaic structure is very serious to an orbit whose F'' is large.

When the amplitude reduction becomes serious at large tilt the Dingle plot will show large non-linearity. In Fig. 15(a) the neck Dingle plots for $\theta_0 = 3^\circ$, 5° , and 6° show increasing curvature.

The calculated Dingle plots, with a $\beta = 0.1^\circ$, also show increasing curvature with tilt [Fig. 15(b)]. However, the root-mean-square deviations (RMSD) of the LSF straight lines to those observed curves are larger by a factor of 2 than those calculated. Those high values of RMSD might be attributed partly to experimental error and partly to the possibility that the mosaic spread of the sample is not just Gaussian. For example, a bicrystal can cause such a large curvature which is a portion of a beat pattern. The emergence of curvature in a Dingle plot at a sufficiently large tilt can be a useful test for substructure in a sample.

The rotation curve can be used to provide further information about the mosaic structure of the sample. Different information may be obtained from its amplitude variation and from its phase variation. In a pure and perfect crystal, the amplitude of the rotation curve varies slowly as a function of orientation owing to the changing of electron effective mass and of the g factor as well as the pickup-coil tilt. In the case of the $\langle 111 \rangle$ neck orbit in Cu, it decreases slowly to its spin-splitting zero (at about 13° away from $\langle 111 \rangle$ along a $\{110\}$ plane). In a real crystal, the amplitude will have an additional variation only if the Dingle temperature is angular dependent. In the case of mosaic structure, X increases very fast with angular tilt and hence the amplitude of the rotation curve will decay quickly. Therefore, one can deduce the *increment* in X along a particular plane at off-symmetry directions using the relation

$$\Delta X = X_a - X_b = -\frac{H}{K_0 \langle m^* \rangle} \ln \left(\frac{V_b}{V_a} \frac{F_a}{F_b} \frac{\cos(\pi g_a m_a^*/2)}{\cos(\pi g_b m_b^*/2)} \right) - \frac{m_b^* - m_a^*}{\langle m^* \rangle} T,$$

where V_a and V_b are the amplitudes at angular tilt θ_a and θ_b from the symmetry direction, respectively, and $\langle m^* \rangle = (m_a^* + m_b^*)/2$. The effect of the pickup-coil tilt was negligible in the range of tilt

TABLE IV. Dingle-temperature increment ($^\circ\text{K}$) as a function of tilt. Results were extracted from the rotation curve of neck oscillation of sample BN5P2-4 at 42 kG. The tilt was measured from $[111]$ along $(\bar{1}10)$ toward $[001]$. In the calculation we have used $g_a = g_b = 1.90$ and assumed a parabolic F , i. e., $F \approx F_0 + F'' \theta^2/2$, where $F'' = 0.78 \times 10^8$ G was determined from the neck rotation curve.

	Tilt	3°	5°	6°
ΔX^{expt}		0.35	0.83	a
ΔX^{calc}	$\beta = 0.12^\circ$	0.27	0.78	1.16
	$\beta = 0.13^\circ$	0.31	0.92	1.36

*Difficult to measure.

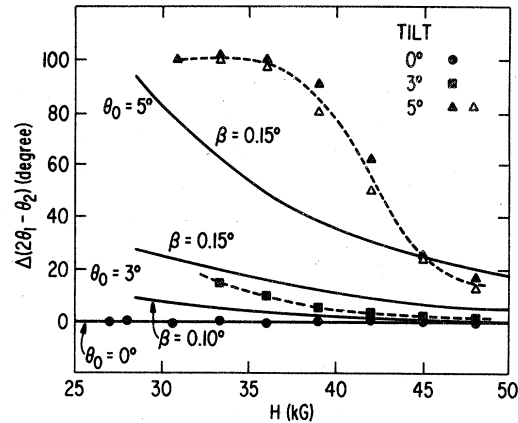


FIG. 16. Relative phase shifts of the $[111]$ neck oscillation of sample BN5P2-4 as a function of field at $\theta_0 = 0^\circ$, 3° , and 5° . The uncertainty is 1° . The constant phase of 45° for the neck from the LK theory has been subtracted from the data. The results at symmetry direction ($\theta_0 = 0^\circ$) are the average from three independent measurements, with slightly different Bessel settings, with a standard error less than 1° for all fields. The results of $\theta_0 = 5^\circ$ are from two independent measurements as shown. Calculated results are shown as solid curves.

considered here. Results of ΔX extracted from the rotation curve of neck oscillation are listed in Table IV. The calculated ΔX are also included for comparison. Although the measured point ΔX cannot be compared directly with the measured slope \bar{X} shown in Fig. 14, it does show some consistency with them. Rotation curves measured at different fields can provide information about the field dependence of the X enhancement.

A useful independent measure of the substructure can be obtained from a rotation diagram of an orbit such as the belly, where F'' is large. The belly rotation diagram of this sample showed a rapid decay in amplitude from $[111]$ and a beat structure consistent with a mosaic spread of $0.10^\circ \pm 0.02^\circ$, both consistent with Fig. 14.

2. Relative phase shift

Strong field- and angular-dependent relative phase shifts, $2\theta_1 - \theta_2$, for the neck orbit were observed and are plotted in Fig. 16. The calculated [Eq. (23)] relative phase shifts, assuming $\beta = 0.1^\circ$ and 0.15° , are shown as solid lines. At the symmetry direction ($\theta_0 = 0^\circ$) the observed relative phase shifts were zero as expected. This is evidence that the magnetic-interaction effect is negligible, as we mentioned earlier. However, at off-symmetry directions the observed results deviated from the calculated curves, especially at larger tilt. This indicates that the actual mosaic spread was not a simple Gaussian. X-ray diffraction measurements were made on this sample.

The data displayed broadened Bragg peaks of complex structure, confirming that the substructure was not pure Gaussian, and with a half-width of 0.1° , in good agreement with four independent dHvA measurements: $\bar{X}(\theta_0)$ (Fig. 14), ΔX from the rotation diagram (Table IV), belly rotation diagrams, and relative phase shifts (Fig. 16).

Both experiment and theory for the neck show large ($\sim 50^\circ$) phase shifts even with relatively small ($\sim 0.1^\circ$) substructure. Those results therefore demonstrate that the relative phase shift is not only a useful way to estimate β but also can be used to distinguish mosaic structure from other amplitude effects because only the phase shifts due to mosaic structure increase so rapidly as the field is tilted from a symmetry direction.

The calculation also indicates that the relative phase shift for the $\langle 111 \rangle$ belly grows very quickly with β even at the symmetry direction. For example, $2\theta_1 - \theta_2$ may be as large as 10° at 30 kG for $\beta = 0.15^\circ$, dropping to 0.03° for $\beta = 0.05^\circ$ at the symmetry direction. Therefore a measurement of the relative phase shift of an orbit which has a large F'' requires a very high perfection of the sample with $\beta \leq 0.05^\circ$ and orientation to the symmetry direction better than 0.1° .

V. DISCUSSION

We have weakened the core effect in our calculation by assuming the strain within a cutoff radius r_0 be equal to that at r_0 . This is justified because the dislocation strain field is long range ($1/r$) and the core area occupies a very small proportion of the average area per dislocation. As mentioned in Sec. III, the dHvA lifetime τ is very sensitive to small-angle scattering and hence to the long-range strain field produced by dislocations. It was found that the calculated results are not sensitive to the choice of r_0 . Recently Martin⁵³ has calculated the scattering due to the core, using a pseudopotential method, and found that the dHvA contribution is genuinely second order. Thus we are justified in concluding that the core contributes a negligible fraction.

Our calculation has not been extended to other orbits than the neck because of the complexity of the orbital integration for noncircular and large ($r_c/d \geq 1$) orbits. We have chosen the phase-smearing parameters (Sec. III B) $\alpha_1 = 15$, $\alpha_2 = -16$, and $\xi = 2$ for the neck orbit throughout the calculation after some initial trials of adjusting these parameters to fit the experimental data. The chosen value for α_1 is larger than that determined from the hydrostatic-pressure experiments^{17,19} by a factor of 4, but in good agreement with that found by CW.¹³ They found the α_1 values to be 15 to 19. The α_2 value agrees very well with that determined from the uniaxial-tensile-stress experiments^{18,20,21}

(which give α_2 of -12 to -16), both in magnitude and in sign. CW did not treat the pure-shear component. (This is equivalent to putting $\alpha_2 = 0$.) A variation in α_1 or α_2 may affect the numerical ratios $\bar{X}_N/\bar{X}_N(111)$ but we find $X(1\bar{1}1) > X(11\bar{1}) > X(\bar{1}11) > X(111)$ in all cases.

Since the precise X values depend on a variety of parameters, we have not attempted to extract precise α values, being content to demonstrate that the dislocation dephasing results are consistent with the strain results. We doubt that the state of strain in the dislocation experiment is sufficiently well defined to enable a quantitative comparison with parameter values. We note that the existing strain results are not sufficient to fully define the parameters needed for the dislocation case: (i) In calculating the four $\langle 111 \rangle$ neck orbits we have assumed that the values of α_1 and α_2 are the same for all orbits, which is not known. (ii) The experimental value of α_2 was determined from uniaxial-tensile-stress measurements in which the tensile axis is parallel to the orbit normal. However, the direction of stress in our strained crystals is parallel to its Burgers vector, i.e., $[101]$, and therefore not directly related to the uniaxial-stress results. (iii) The strain ($\sim 10^{-2}$, easy-glide region) in our crystals is much larger than the strain (10^{-4} , elastic region) used in those measurements, and we have no evidence that the strain phase shift is linear at such large strains.

The lattice model used in our calculation is rather realistic for our pure crystals, since in such a crystal dislocations are highly mobile (in single slip) and rapidly glide to minimum-energy configuration, which is the array we have adopted. Although our earlier work¹⁰ (with less-pure samples) showed a more random array (due to the presence of pinning sites), the micrographs of the present very pure and nearly perfect crystals clearly exhibit a correlated array [see slip lines in Fig. 3(b)].

Although the assumption of coherence for the calculation of a periodic dislocation array will almost certainly lead to an overestimate of the net dephasing, the overestimate need not be large. It is illustrative to compare with the calculation of Coleridge⁵⁴ of the strain dephasing due to size mismatch of an impurity. The original calculation had a coherent matching of contributions from different impurities sampled along the electron orbit. This led to an overestimate⁵⁵ of the dephasing compared to a random array, of essentially N/\sqrt{N} , where N is the number of impurities along the circumference. This amounts to nearly a factor of 10 in the situation considered. In the dislocation case, the overestimate is not likely to be so large since (i) the array was chosen to correspond with observed dislocation arrays, which are

far from random; (ii) because the strain field is antisymmetric, there is a good deal of cancellation of dephasing *within* the range of a given dislocation, whereas the impurity dephasing is always in the same direction; (iii) the number of dislocations sampled by a given orbit is small (~ 1), so that N and \sqrt{N} do not differ by a large factor.

Kaner and Feldman⁵⁶ have studied the Landau-level structure in the presence of dislocations, and conclude that sublevels will appear. No effects attributable to such sublevels have been observed in this experiment. However, Kaner and Feldman used a δ -function potential, with no long-range strain field. This is equivalent to a core-scattering calculation only, and we suggest that sublevel effects are therefore unobservable in this case owing to the overwhelming dominance of the long-range strain field. Measurement of cyclotron-resonance spectra in unstrained and strained tellurium crystals with a dislocation density of 10^5 and 10^8 cm^{-2} also gave no indication of additional transitions due to sharp dislocation sublevels up to 10 MeV above the valence-band edge in magnetic fields up to 56 kG.⁵⁷

In another attempt, Kaner and Feldman⁵⁸ have assumed that the interaction of an electron with dislocations is due to a long-range deformation potential of the lattice and showed the existence of additional energy bands—dislocation bands—in the electron energy spectrum. The width of the dislocation band is of the order of $\Lambda b N_d^{1/2}$, where Λ is the deformation-potential constant. Based on these results Gutnikov and Feldman⁵⁹ have derived the Dingle temperature, in the limit $r_c/d \ll 1$, and found

$$X_r = \frac{2\pi^2 r H}{K_0 m^*} \left(\frac{\Lambda b N_d^{1/2}}{\hbar \omega_c} \right)^2 = m^* \Lambda^2 b^2 \frac{r N_d}{H}. \quad (25)$$

Hence the Dingle temperature is linearly dependent on the dislocation density N_d and the harmonic index r and inversely proportional to the magnetic field H . The scattering anisotropy will depend on the factor $m^* \Lambda^2$ and hence is related to the anisotropy of the deformation potential. For a free-electron gas the deformation potential would be isotropic and equal to $2E_F/3$, which is 4.99 eV for copper.

An estimate based on Eq. (25) is of the same magnitude as the observed results. In noble metals the deformation potentials for shear strains have been calculated only at high-symmetry points.^{60,61} Using the deformation potential calculated at the symmetry point $L(\frac{1}{2}, \frac{1}{2}, \frac{1}{2})$ under trigonal strain as the deformation potential for the neck orbit, an estimate of X from Eq. (25) for a N_d of 10^7 cm^{-2} gives 0.63 °K (30 kG) to 0.38 °K (50 kG) for X_1 . These values have the same order of magnitude as the experimental results. However, the strong $(1/H)$ field dependence is against the experimental evidence. This is not surprising since the $1/H$ field dependence of X is a consequence of the assumed random spacing.⁵⁸ Besides, the angle between the direction of dislocations and the magnetic field was not entered in the original derivation by Gutnikov and Feldman, and the deformation potential used to estimate X was calculated for a stress direction differing from that in our strained crystals. Therefore, more theoretical and experimental work on the deformation potential for the appropriate shear strain is needed in order to make further comparisons between Eq. (25) and the detailed ex-

TABLE V. Comparison of the assumptions and steps used in the phase-smearing calculations of the present work with those used by Watts (Ref. 14).

	Watts	Present work
Strain field ^a	(a) volume (Δ) (b) rotation (w)—found negligible	(a) volume (Δ) + shear (ϵ) rotation (w) is neglected (b) mosaic structure
Direction of dislocations	random (all slip systems)	parallel (single slip)
Strain distribution	Gaussian is assumed	using strain-field expressions from elastic theory; periodic array
Core	neglected (10 Å)	flat (10 Å)
Orbit strain sensitivity parameters	$\mu\Delta$	$\alpha_1\Delta + \alpha_2\epsilon$
Orbit averaging	incoherent (after sample averaging)	coherent (before sample averaging)
Sample averaging	small N_d : constant strain large N_d : Gaussian correlation	slip-line model (parameter ξ)

^aOnly (a) was treated in the main calculation; (b) was treated separately.

perimental results presented here.

The other principal dislocation-scattering calculation using a dephasing approach is that due to Watts.¹⁴ The principal differences between our two approaches is summarized in Table V. Using an assumed Gaussian strain distribution, Watts showed that the X values are consistent with experiment, using the results of pressure measurements as parameters. The present calculation is an attempt to improve upon that approach, with a first-principles dephasing calculation. Absent in our results is certain systematic behavior, which is a consequence of the Gaussian assumption, and which so far at least has not shown up in experiment. This includes a strongly field-dependent scattering, and a strongly nonlinear dependence of X upon N_d . Our calculation shows no simple field dependence, and a weakly nonlinear dependence upon N_d . The linear array of dislocations used is close to the experimental array, and allows exploration of broken-cubic-symmetry effects.

After this work was completed,³⁹ it came to our attention that Watts⁶² has formulated the dephasing calculation and independently shown the equivalence between dephasing and small-angle scattering by a different approach. We note an error in Ref. 62 which, however, does not affect the fundamental connection between scattering and dephasing. An erroneous scaling law relates phase changes for the various dHvA harmonics. Equations (14), (19), and (29) of Ref. 62 state

$$\psi_r(H) = \psi_1(H/r),$$

leading to

$$X_r(H) = X_1(H/r).$$

This is in error, since the strain field sampled by an orbit (and hence the phase change) is field dependent, owing to the change with field of orbit size. Our calculated results (Fig. 9) demonstrate clearly $X_2(H) \neq X_1(H/2)$.

TABLE VI. Comparison of dislocation scattering results in copper from different experimental methods. Data shown are for a dislocation density of 10^7 cm^{-2} . The scattering cross sections are given in b , the magnitude of a unit Burgers vector.

	Critical angle θ_c (deg)	τ^{-1} (sec ⁻¹)	Scattering cross section (b)
dHvA	0.01	7×10^{10}	2000
RFSE	1	2×10^9	60
Resistivity	~ 45	4×10^7 5×10^8 ^a	1 13 ^a

^aFrom Ref. 8.

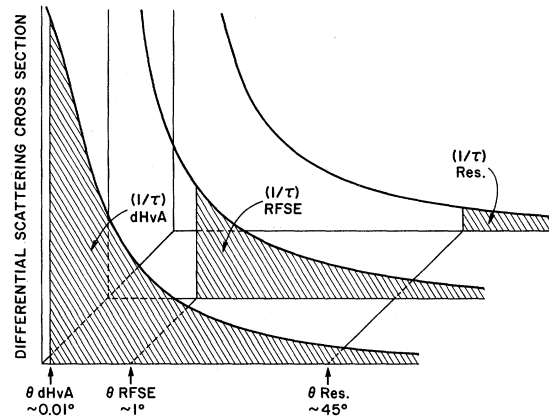


FIG. 17. Comparison of dislocation scattering results in copper from different experimental methods.

One intriguing sidelight of having more than one way to measure a lifetime is that differences between the results of different methods can be used to say something about the angular nature of the scattering cross section.⁶³ For example, in the case of dislocation scattering, there are now three different measurements that we are aware of: resistivity, dHvA, and radio-frequency size-effect⁸ (RFSE) results. A comparison of the magnitudes shows that the cross section is very strongly peaked in the forward direction; i. e., most of the scattering is small angle. The comparison is rough but the effect is so strong that the result is very striking. The comparison is given in Table VI, measured for a dislocation density of 10^7 cm^{-2} . We have chosen the belly-orbit data to represent dHvA and RFSE results, because belly electrons represent a greater part of the FS and have a primary contribution to the electrical resistivity.

In comparing the results of these three measurements, we are comparing techniques in which the critical angle above which a scattering event is destructive is very different. This critical angle θ_c is less than 0.01° for belly orbits in dHvA. Gantmakher notes a critical angle in RFSE of about 1° , a factor of 100 larger. In resistivity, if one argues that the dominant angular factor is $1 - \cos\theta$, then only scattering events of larger than about 45° are important. For impurity scattering, or other event in which the scattering is relatively isotropic, the distinction is relatively unimportant, and amounts to at most a factor of 2. In dislocation scattering, the experimental $1/\tau$ results differ by a total of three orders of magnitude, and the notion of the critical angle may go part of the way in explaining it. The large value obtained for the dHvA scattering cross section suggests that the differential scattering cross section must be strongly peaked in the forward direction (Fig. 17), and one

can infer that in the dHvA effect every scattering event counts and hence it measures the *total* scattering cross section, averaged over a selected part of the FS, in contrast to the resistivity, in which an electron scattered off its path may still make contribution to the electron flux.

The discrepancy between the theoretical and experimental dislocation resistivity ρ_d still remains, and amounts to a factor of 10.^{1,2} Most of these measurements were done on high dislocation densities, $N_d \geq 10^9 \text{ cm}^{-2}$, produced by tension or rolling. At such high densities dislocations are correlated to a large extent. This correlated effect may bring large cancellation among strain fields and hence reduce the value of ρ_d/N_d in the work hardening region.^{6,7} Another factor which may contribute to this discrepancy is the uncertainty inherent in the sample preparation and defect characterization.⁷ Therefore, to study well-defined dislocations will be more useful to resolve this controversy. Observed values of ρ_d/N_d on well-defined dislocations^{6,8} do show anisotropy and dislocation configuration dependence as we have found in the present work. Gantmakher *et al.* have obtained a scattering cross section, from their resistivity measurements on well-defined dislocations, of $13b$ compared to $1b$ obtained from most of the earlier resistivity measurements. Note that the core of a dislocation is of order of $1b$. These results strongly suggest that the dislocation resistivity may as well be strongly affected by the long-range strain field.

The problem of phase smearing because of mosaic structure has been discussed previously,^{9,31,51} and can lead to serious errors in any scattering measurement. Miller *et al.*⁶⁴ have illustrated the importance of the effect of mosaic structure on the off-symmetry Dingle-temperature measurements on an AuCu alloy. They corrected the enhancements due to mosaic structure until it achieved a self-consistency in the electronic lifetime mapping. In the present work, we have directly measured the characteristic mosaic-spread half-width β using several independent measurements and found good agreement among them. Furthermore, we have been first to study the relative phase shift due to mosaic structure both experimentally and theoretically.

VI. SUMMARY

Effects of dislocation strain and mosaic structure on conduction electrons have been studied using

the dHvA effect. The results have been found to be in good agreement with the phase-smearing calculation using simple models both in amplitude reduction and in relative phase shift. There is a large Dingle-temperature anisotropy (up to a factor of 2) among four $\langle 111 \rangle$ neck orbits. This is a result of the plane strain field produced by dislocations. An even larger anisotropy was observed among different orbits (largest for the dog bone, rosette, and neck, and smaller for the bellies). This indicates that those orbits that are in contact with the BZ boundary suffer large fractional changes in FS cross sections under stress and hence large amplitude reductions. It was also demonstrated that the traditional (slope) Dingle temperature measured from the H dependence of the amplitude does not provide a direct measure of point Dingle temperature when the point Dingle temperature has a field dependence. The large discrepancy between the experimental $1/\tau$ results measured by dHvA, RFSE, and resistivity methods is attributed to the sensitivity of the specific method to small-angle scattering by the long-range strain field around dislocations.

The results of this work also indicate the importance of sample preparation in the dHvA measurements. We have demonstrated several methods to detect and measure mosaic structure. The strong angular and field dependence of the relative phase shift as well as the strong angular dependence of X due to mosaic structure are useful in determining the mosaic structure and in separating its influence, which is often unwanted and annoying, from other effects. It has also been demonstrated that the rotation curve can be used as a quick and reliable way to measure angular dependence of X enhancement as well as determining the mosaic structure.

ACKNOWLEDGMENTS

We thank H. G. Alles for helpful discussions on the automated dHvA data-acquisition system, J. W. McClure and A. Seeger for helpful discussions, and J. W. Martin for sending us the results of his dislocation scattering calculation. One of us (Y. K. C.) acknowledges support from the U. S. Atomic Energy Commission while a portion of this manuscript was written at Argonne National Laboratory.

*Research supported by the National Science Foundation.

†Present address: Argonne National Laboratory, Argonne, Ill. 60439.

¹J. M. Ziman, *Adv. Phys.* **13**, 89 (1964); in *The Physics of Metals, Vol. 1, Electrons*, edited by J. M. Ziman (Cambridge U.P., New York, 1969), p. 264.

²F. R. N. Nabarro, *Theory of Crystal Dislocations* (Oxford U.P., London, 1967), Sec. 9.2.

³Z. S. Basinski and S. Saimoto, *Can. J. Phys.* **45**, 1161 (1967).

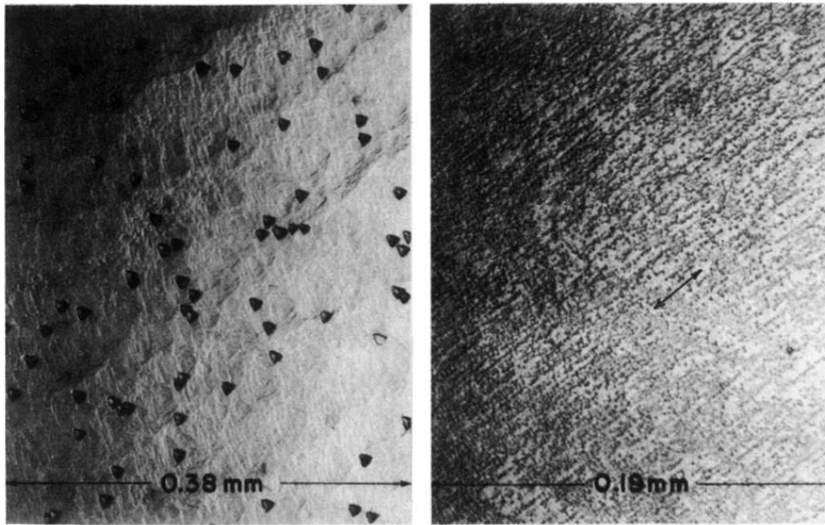
⁴R. A. Brown, *Phys. Rev.* **156**, 692 (1967).

⁵A. B. Bhatia and O. P. Gupta, *Phys. Rev. B* **1**, 4577 (1970).

⁶H. Yoshinaga, *Phys. Status Solidi* **18**, 625 (1966).

⁷O. Buck, D. Schumacher, and A. Seeger, *Phys. Status Solidi B* **60**, 707 (1973).

- ⁸V. F. Gantmakher, V. F. Gasparov, G. I. Kulesko, and V. N. Matveev, *Zh. Eksp. Teor. Fiz.* **63**, 1752 (1972) [*Sov. Phys. -JETP* **36**, 925 (1973)].
- ⁹D. Shoenberg, *Phys. Kondens. Mater.* **9**, 1 (1969).
- ¹⁰D. W. Terwilliger and R. J. Higgins, *Phys. Rev. B* **7**, 667 (1973).
- ¹¹D. W. Terwilliger and R. J. Higgins, *Phys. Lett. A* **31**, 316 (1970).
- ¹²R. J. Higgins, D. W. Terwilliger, and Y. K. Chang, in *Low Temperature Physics—LT 12*, edited by E. Kanda (Keigaku, Tokyo, 1970), p. 605.
- ¹³P. T. Coleridge and B. R. Watts, in *Low Temperature Physics—LT 12*, edited by E. Kanda (Keigaku, Tokyo, 1970), p. 611; *Philos. Mag.* **24**, 1163 (1971).
- ¹⁴B. R. Watts, in *Low Temperature Physics—LT 12*, edited by E. Kanda (Keigaku, Tokyo, 1970), p. 609; *Philos. Mag.* **24**, 1151 (1971).
- ¹⁵R. J. Higgins, H. Alles, Y. K. Chang, and D. W. Terwilliger, in *Low Temperature Physics—LT 13*, edited by K. D. Timmerhaus, W. J. O'Sullivan, and E. F. Hammel (Plenum, New York, 1974), Vol. 4, p. 185.
- ¹⁶A. B. Pippard, *Proc. R. Soc. A* **287**, 165 (1965).
- ¹⁷I. M. Templeton, *Proc. R. Soc. A* **292**, 413 (1966); *Can. J. Phys.* **52**, 1628 (1974).
- ¹⁸D. Shoenberg and B. R. Watts, *Philos. Mag.* **15**, 1275 (1967).
- ¹⁹W. J. O'Sullivan and J. E. Schirber, *Phys. Rev.* **170**, 667 (1968).
- ²⁰P. R. Aron, *J. Low Temp. Phys.* **9**, 67 (1972).
- ²¹A. J. Slavin, *Philos. Mag.* **27**, 65 (1973).
- ²²H. G. Alles and R. J. Higgins, *Phys. Rev. B* **9**, 158 (1974).
- ²³I. M. Lifshitz and A. M. Kosevich, *Zh. Eksp. Teor. Fiz.* **29**, 730 (1955) [*Sov. Phys. -JETP* **2**, 636 (1956)].
- ²⁴A. V. Gold, in *Solid State Physics, Volume 1, Electrons in Metals*, edited by J. F. Cochran and R. R. Haering (Gordon and Breach, New York, 1968), pp. 39–126.
- ²⁵D. Shoenberg and P. J. Stiles, *Proc. R. Soc. A* **281**, 62 (1964).
- ²⁶R. W. Stark and L. R. Windmiller, *Cryogenics* **8**, 272 (1968).
- ²⁷L. R. Windmiller and J. B. Ketterson, *Rev. Sci. Instrum.* **39**, 1672 (1968).
- ²⁸H. G. Alles, Ph.D. thesis (University of Oregon, 1972) (unpublished).
- ²⁹H. G. Alles and R. J. Higgins, *Rev. Sci. Instrum.* (to be published).
- ³⁰H. G. Alles and R. J. Higgins, *Rev. Sci. Instrum.* **44**, 1646 (1973).
- ³¹D. Shoenberg, *Philos. Trans. R. Soc. Lond. A* **255**, 85 (1962).
- ³²H. G. Alles, Y. K. Chang, R. J. Higgins, and J. Nosler (unpublished).
- ³³J. J. Gniewek and A. F. Clark, *J. Appl. Phys.* **36**, 3358 (1965).
- ³⁴D. W. Terwilliger and R. J. Higgins, *J. Appl. Phys.* **43**, 3346 (1972).
- ³⁵U. Bonse, E. Kappler, and W. Velhoff, *Phys. Status Solidi* **3**, K355 (1963).
- ³⁶E. M. Porbansky, *Trans. Metall. Soc. AIME* **230**, 925 (1964).
- ³⁷F. W. Young, Jr. and J. R. Savage, *J. Appl. Phys.* **35**, 1917 (1964).
- ³⁸L. D. Dyer, *J. Appl. Phys.* **36**, 301 (1965).
- ³⁹Y. K. Chang, Ph.D. thesis (University of Oregon, 1974) (unpublished); a portion of this was presented in *Bull. Am. Phys. Soc.* **19**, 249 (1974).
- ⁴⁰C. Barrett and T. B. Massalski, *Structure of Metals*, 3rd ed. (McGraw-Hill, New York, 1966), p. 210.
- ⁴¹F. W. Young, Jr. and T. R. Wilson, *Rev. Sci. Instrum.* **32**, 559 (1961).
- ⁴²J. D. Livingston, *J. Appl. Phys.* **31**, 1071 (1960).
- ⁴³J. D. Livingston, in *Direct Observation of Imperfections in Crystals*, edited by J. B. Newkirk and J. H. Wernick (Interscience, New York, 1962), p. 115.
- ⁴⁴W. T. Read, Jr., *Acta Metall.* **5**, 83 (1957).
- ⁴⁵R. D. Dingle, *Proc. R. Soc. A* **211**, 517 (1952).
- ⁴⁶A. D. Brailsford, *Phys. Rev.* **149**, 456 (1966).
- ⁴⁷E. Mann, *Phys. Kondens. Mater.* **12**, 210 (1971).
- ⁴⁸J. M. Ziman, *Principles of the Theory of Solids* (Cambridge U.P., Cambridge, England, 1964), p. 187.
- ⁴⁹A. B. Pippard, in *Solid State Physics, Vol. 1, Electrons in Metals*, edited by J. F. Cochran and R. R. Haering (Gordon and Breach, New York, 1968), p. 1.
- ⁵⁰The absolute phase shift is usually difficult to measure because the absolute phase in noble metals is very high. However, the relative phase shift between the first and second harmonic, $2\theta_1 - \theta_2$, is measurable, using wave-shape analysis of dHVA signals.
- ⁵¹M. G. Priestley, *Philos. Mag.* **7**, 1205 (1962).
- ⁵²M. R. Halse, *Phil. Trans. R. Soc. Lond. A* **265**, 507 (1969).
- ⁵³J. W. Martin (private communication); method similar to J. W. Martin and J. M. Ziman, *J. Phys. C* **3**, L75 (1970).
- ⁵⁴P. T. Coleridge, *Philos. Mag.* **26**, 573 (1972).
- ⁵⁵P. T. Coleridge, *Philos. Mag.* **27**, 1495 (1973).
- ⁵⁶E. A. Kaner and E. P. Feldman, *Zh. Eksp. Teor. Fiz.* **58**, 1803 (1970) [*Sov. Phys. -JETP* **31**, 966 (1970)].
- ⁵⁷M. V. Ortenberg, *Phys. Status Solidi B* **60**, 531 (1973).
- ⁵⁸E. A. Kaner and E. P. Feldman, *Zh. Eksp. Teor. Fiz.* **61**, 419 (1971) [*Sov. Phys. -JETP* **34**, 222 (1972)].
- ⁵⁹A. I. Gutnikov and E. P. Feldman, *Zh. Eksp. Teor. Fiz.* **63**, 1054 (1972) [*Sov. Phys. -JETP* **36**, 553 (1973)].
- ⁶⁰G. E. Juras and B. Segall, *Phys. Rev. Lett.* **29**, 1246 (1972); *Surf. Sci.* **37**, 929 (1973).
- ⁶¹A. M. Gray, D. M. Gray, and E. Brown, *Phys. Rev. B* **11**, 1475 (1975).
- ⁶²B. R. Watts, *J. Phys. F* **4**, 1371 (1974).
- ⁶³The scattering cross section for dislocation has a dimension of length, and hence is often called the scattering width or scattering diameter.
- ⁶⁴K. M. Miller, R. G. Poulsen, and M. Springford, *J. Low Temp. Phys.* **6**, 411 (1972).



(a)

(b)

FIG. 3. Etch-pit micrographs on the (111) surface of crystal BN5P2. (a) Unstrained; $N_d \approx 3 \times 10^4 \text{ cm}^{-2}$. (b) Bent and straightened; $N_d \approx 2 \times 10^7 \text{ cm}^{-2}$. The arrow indicates the slip direction.